Cancer Cell

Article

Myeloid cell networks govern re-establishment of original immune landscapes in recurrent ovarian cancer

Graphical abstract

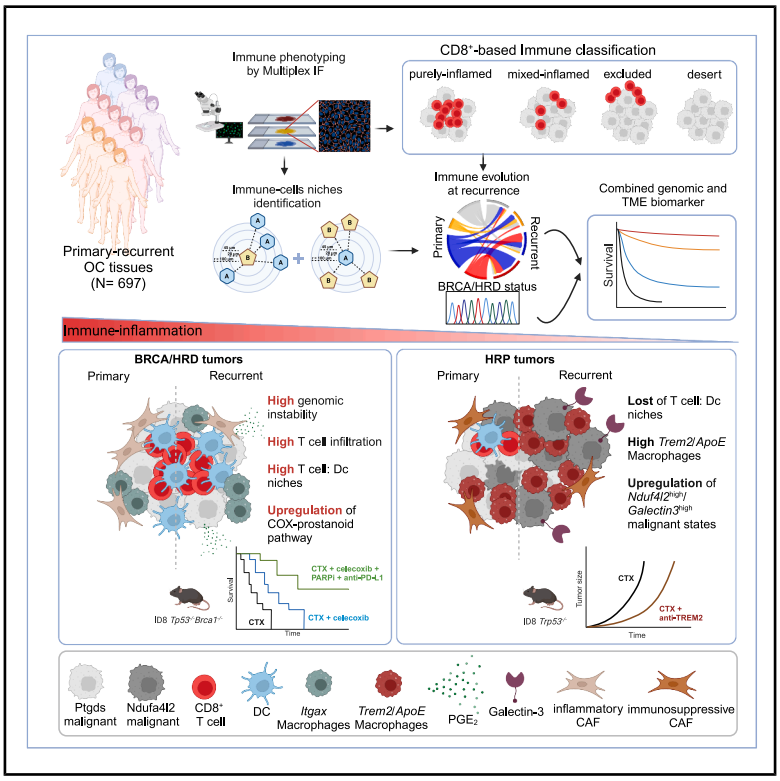

Highlights

- Ovarian cancer (OC) profiling identifies four immune phenotypes predictive of prognosis
- HRD status and TIL:myeloid niches shape the immune landscape at OC recurrence
- Recurrent HRD OCs evade immunity via COX/PGE_2 signaling
- TREM2 blockade enhances chemotherapy responses in *Brca1*^{wt} OC models

Authors

Eleonora Ghisoni, Fabrizio Benedetti, Aspram Minasyan, ..., Christina Fotopoulou, Jose R. Conejo-Garcia, Denarda Dangaj Laniti

Correspondence

denarda.dangaj@chuv.ch

In brief

Ghisoni et al. profile the immune landscape of 697 ovarian cancers (OCs), identifying four immune phenotypes linked to prognosis and treatment response. The study demonstrates that BRCA-dependent TIL:myeloid interactions drive immunogenicity at OC recurrence. It provides new therapeutic vulnerabilities and biomarkers to improve selection and clinical outcomes for OC patients.

Ghisoni et al., 2025, Cancer Cell *43*, 1568–1586
August 11, 2025
https://doi.org/10.1016/j.ccell.2025.07.005

CellPress

CellPress
OPEN ACCESS

Cancer Cell

Article

Myeloid cell networks govern re-establishment of original immune landscapes in recurrent ovarian cancer

Eleonora Ghisoni,[1,2] Fabrizio Benedetti,[1,21] Aspram Minasyan,[1,21] Mathieu Desbuisson,[1] Paula Cunnea,[3] Alizée J. Grimm,[1] Noémie Fahr,[1] Charlotte Capt,[1] Nicolas Rayroux,[1] Flavia De Carlo,[1] Doga C. Gulhan,[1,4] Julien Dagher,[5] David Barras,[1] Matteo Morotti,[1] Juan A. Marín-Jiménez,[6] Bovannak Stewen Chap,[1] Tania Santoro,[1] Giulia Spagnol,[7] Mapi Fleury,[2] Katerina Fortis,[8] Julien Dorier,[9] Mary K. Townsend,[10] Stephanie Tissot,[8] Sylvie Rusakiewicz,[8] Humberto J. Ferreira,[1] Anne I. Kraemer,[1] Michal Bassani-Stenberg,[1] Elizabeth M. Swisher,[11] Lana A. Kandalaft,[1,8] Spyridon A. Mastroyannis,[12] Kathleen T. Montone,[13] Daniel J. Powell, Jr.,[13] Susana Banerjee,[14] Kathryn L. Terry,[15,16] Shelley S. Tworoger,[10] Mikaël J. Pittet,[1,17] Janos L. Tanyi,[12] George Coukos,[1,2] Melissa A. Merritt,[18,19] Christina Fotopoulou,[3] Jose R. Conejo-Garcia,[20] and Denarda Dangaj Laniti[1,22,*]

[1]Department of Oncology, Lausanne University Hospital; Ludwig Institute for Cancer Research, Lausanne Branch, University of Lausanne (UNIL); Agora Cancer Research Center, Lausanne, Switzerland
[2]Immuno-oncology Service, Department of Oncology, Lausanne University Hospital, Lausanne, Switzerland
[3]Division of Cancer, Department of Surgery and Cancer, Imperial College London, London W12 0HS, UK
[4]Massachusetts General Hospital Cancer Center and Harvard Medical School Department of Medicine, Boston, MA, USA
[5]Unit of Translational Oncopathology, Institute of Pathology, Lausanne University Hospital, Lausanne, Switzerland
[6]Cancer Immunotherapy Group, Bellvitge Biomedical Research Institute (IDIBELL), L'Hospitalet de Llobregat, Barcelona, Spain
[7]Department of Women and Children's Health, Unit of Gynecology and Obstetrics, University of Padua, Padua, Italy
[8]Center of Experimental Therapeutics, Department of Oncology, Lausanne University Hospital, Lausanne, Switzerland
[9]Bioinformatics Competence Center, University of Lausanne, Lausanne, Switzerland
[10]Division of Oncological Sciences, OHSU Knight Cancer Institute, Portland, OR, USA
[11]Department of Obstetrics/Gynecology, University of Washington, Seattle, WA, USA
[12]Ovarian Cancer Research Center, University of Pennsylvania, Philadelphia, PA 19104, USA
[13]Department of Pathology and Laboratory Medicine, University of Pennsylvania, Philadelphia, PA 19104, USA
[14]The Royal Marsden NHS Foundation Trust and Institute of Cancer Research, London, UK
[15]Obstetrics and Gynecology Epidemiology Center, Department of Obstetrics and Gynecology, Brigham and Women's Hospital and Harvard Medical School, Boston, MA, USA
[16]Department of Epidemiology, Harvard T.H. Chan School of Public Health, Boston, MA, USA
[17]Department of Pathology and Immunology, University of Geneva, Geneva, Switzerland
[18]The Daffodil Centre, The University of Sydney, a joint venture with Cancer Council NSW, Sydney, NSW, Australia
[19]Faculty of Medicine and Health, The University of Sydney, Sydney, NSW, Australia
[20]Department of Integrative Immunobiology, Duke School of Medicine, Durham, NC 27707, USA
[21]These authors contributed equally
[22]Lead contact
*Correspondence: denarda.dangaj@chuv.ch
https://doi.org/10.1016/j.ccell.2025.07.005

SUMMARY

Immunotherapy has shown limited success in recurrent ovarian cancer (OC), with prognostic insights largely derived from treatment-naive tumors. We analyzed 697 tumor samples (566 primary and 131 recurrent) from 595 OC patients across five independent cohorts, capturing tumor-infiltrating lymphocytes (TILs) heterogeneity and identifying four immune phenotypes linked to prognosis and TIL:myeloid networks driving malignant progression. We found that in preclinical mouse models, mirroring inflamed human OCs, the recurrent *Brca1*^{mut} tumors maintained activated TILs:dendritic cells (DCs) niches but evaded immune control through upregulation of COX/PGE_2 signaling. Conversely, recurrent *Brca1*^{wt} tumors displayed loss of TILs:DCs niches and accumulated immunosuppressive tumor microenvironment (TME) networks featuring *Trem2/ApoE*^{high} tumor associated macrophages (TAMs) and *Nduf4l2*^{high}/*Galectin3*^{high} malignant states. Recurrent tumors recapitulate the immunogenic landscapes of original cancers. Our findings reveal BRCA-dependent TIL:myeloid crosstalk as key to persistent immunogenicity in recurrent OC and propose new targets to enhance chemotherapy efficacy.

INTRODUCTION

Ovarian cancer (OC) is the leading cause of death from gynecological malignancies.[1] Despite optimal front-line treatment (cytoreductive surgery and platinum-based chemotherapy, CTX), most women with advanced-stage disease will ultimately relapse. Life expectancy for platinum-resistant patients does not exceed one year, and new treatment options are urgently needed to increase response rate and survival.[2]

About half of the patients with OC contain tumor-infiltrating lymphocytes (TILs) within tumor islets, and the presence of intra-epithelial (ie)TILs in primary tumors correlates with overall survival (OS).[3–5] Moreover, tumors which harbor homologous recombination deficiency (HRD) have a higher neo-antigen load, more TILs, and up-regulation of programmed cell death protein-1 and its ligand (PD1/PD-L1) immune axis.[6,7] Despite being considered as a potential therapeutic option for OC, immune-checkpoint inhibitors (ICIs) have fallen short of expectations with no agent approved so far.[8,9] Additionally, potential biomarkers like PD-L1 expression, tumor mutational burden and TILs have yet to be proven predictive for patient selection.[10] Although the presence and state of TILs in OC have been extensively explored in previous studies,[11–14] recent research has shed light on the involvement of additional immune cell types in sculpting the tumor microenvironment (TME) of OC.[15–18] However, a comprehensive understanding of the temporal evolution of immune cell infiltration and its spatial organization in the recurrent disease setting is still lacking.[13]

Disease progression after standard-of-care therapy can lead to immune-exclusion and therapeutic failure.[12,19–22] Considering the poor outcomes of ICIs/CTX combination in the most recent trials,[23–25] it is debatable whether CTX and ICIs can effectively collaborate to promote tumor control in OC, despite quasi-universal consensus about OC immunogenicity.

In this study, we employed digital pathology to capture the heterogeneity of $CD8^+$ T cell infiltration among the largest multi-institutional collection of OC primary-recurrent samples so far, accounting for 697 tumor samples from 595 patients. We observed significant immune and molecular heterogeneity in tumor immune phenotypes and their dynamics during disease recurrence. To mechanistically disentangle the evolution of the TME at tumor progression, we translated the clinical standard-of-care treatment of OC in preclinical syngeneic mouse *Brca1* isogenic OC models and comparatively characterized the evolution of their malignant and TME states. Our study underlines mechanisms dictating the course of immunogenic evolution of $BRCA1^{mut}$ and homologous recombination proficient (HRP) tumors and provides new therapeutic vulnerabilities and biomarkers to improve selection and clinical outcomes for OC patients.

RESULTS

Intra-tumoral heterogeneity of TILs infiltration in OC reveals four $CD8^+$ immune phenotypes associated with differential prognosis

We analyzed a total of 697 OC samples from five independent clinical cohorts with matching treatment-naive and recurrent tumors (Figure 1A, STAR Methods). Given the absence of standardized methods for $CD8^+$ T cell quantification by multiplex immunofluorescence (mIF), we built an algorithm able to capture the heterogeneity of $CD8^+$ T cell densities and their spatial distribution in whole-tissue slides. We converted the established mean of five $ieCD8^+$ T cells per high-power field captured by standardized IHC[3,4] to a mean of 21 $ieCD8^+$ T cells/mm^2 quantified by mIF on whole FFPE slides (Figure 1B). We tested the strength of this new $CD8^+$ T cell density cut-off to discriminate OS in primary tumors from two of our clinical cohorts (IMCOL, Table S1A and UPENN; Table S1B). Patients with tumors infiltrated by a mean of >21 $ieCD8^+$ T cells/mm^2 had significantly longer OS than those with <21 $ieCD8^+$ T cells/mm^2 (Figure 1C) even after adjusting for optimal residual disease (R = 0) at first surgery (Figure S1A). While our new mIF-based cut-off separates long-term survivors, it still represents a mean density of $CD8^+$ TILs and therefore ignores the observed heterogeneity across surgical specimens (Figure S1B). Thus, we segmented tissues in equal sub-regions (or regions of interest, ROIs) to cover the entire FFPE slide. We annotated tumor and stroma regions within each ROI based on pan-cytokeratin (CK^+) expression and applied our new $CD8^+$ T cell density cut-off (21 $CD8^+$ cells/mm^2) to each ROI (Figure S1C and STAR Methods). We identified four different immune phenotypes in treatment-naive OC: purely inflamed, mixed-inflamed, excluded, and desert tumors according to the percentage of ROIs exhibiting >21 $CD8^+$ cells/mm^2 in the intra-tumoral or stromal compartment (Figures 1D and S1C). We interrogated the prevalence of these four immune phenotypes in the primary tissues of our two training cohorts (Figure 1E) and observed differences which could be explained by characteristics such as stage, optimal debulking rates and platinum-free interval (Figure S1D; Tables S1A and S1B). Importantly, our immune phenotype classifier significantly correlated with clinical outcome, as patients with purely and mixed-inflamed phenotypes had a statistically significant longer OS compared to those with excluded and desert tumors (Figure 1F). Then we applied our immune classifier to a third, independent OC collection (HiTide-UPENN, Figure 1G; Table S2A). Consistently, long-term survivors were those with purely and mixed inflamed tumors (Figure 1H). As a further validation, we applied our CD8 immune classifier on a large OC tissues microarray (TMA) cohort from the Nurses Health Study (NHS) and NHSII[26,27] including 418 patients (Figures 1I and 1J and STAR Methods). By integrating data from mIF protein panels staining for CD8, we captured four immune phenotypes similarly to what we showed in our whole-slide OC tissue collection (Figure S1C). Furthermore, we assessed the association of these 4 immune classes with survival in the NHS cohort by taking into statistical consideration covariates, such as tumor subtype, stage, age, and year of diagnosis. We showed that patients with mixed inflamed, excluded, and desert tumors had increased hazard ratios for death compared to purely inflamed ones (Figure 1K).

Collectively our data suggest that long-term OC survivors are those with purely and mixed inflamed tumors. As expected, immune inflammation was partly associated with HRD status. BRCA/HRD OC was significantly enriched in inflamed tumors while excluded and desert immune phenotypes were more abundant in HRP OCs (Figures S1E and S1F and STAR Methods). Beyond the immune inflammatory state, genomic alterations, such as those which cause HRD, and chromosomal

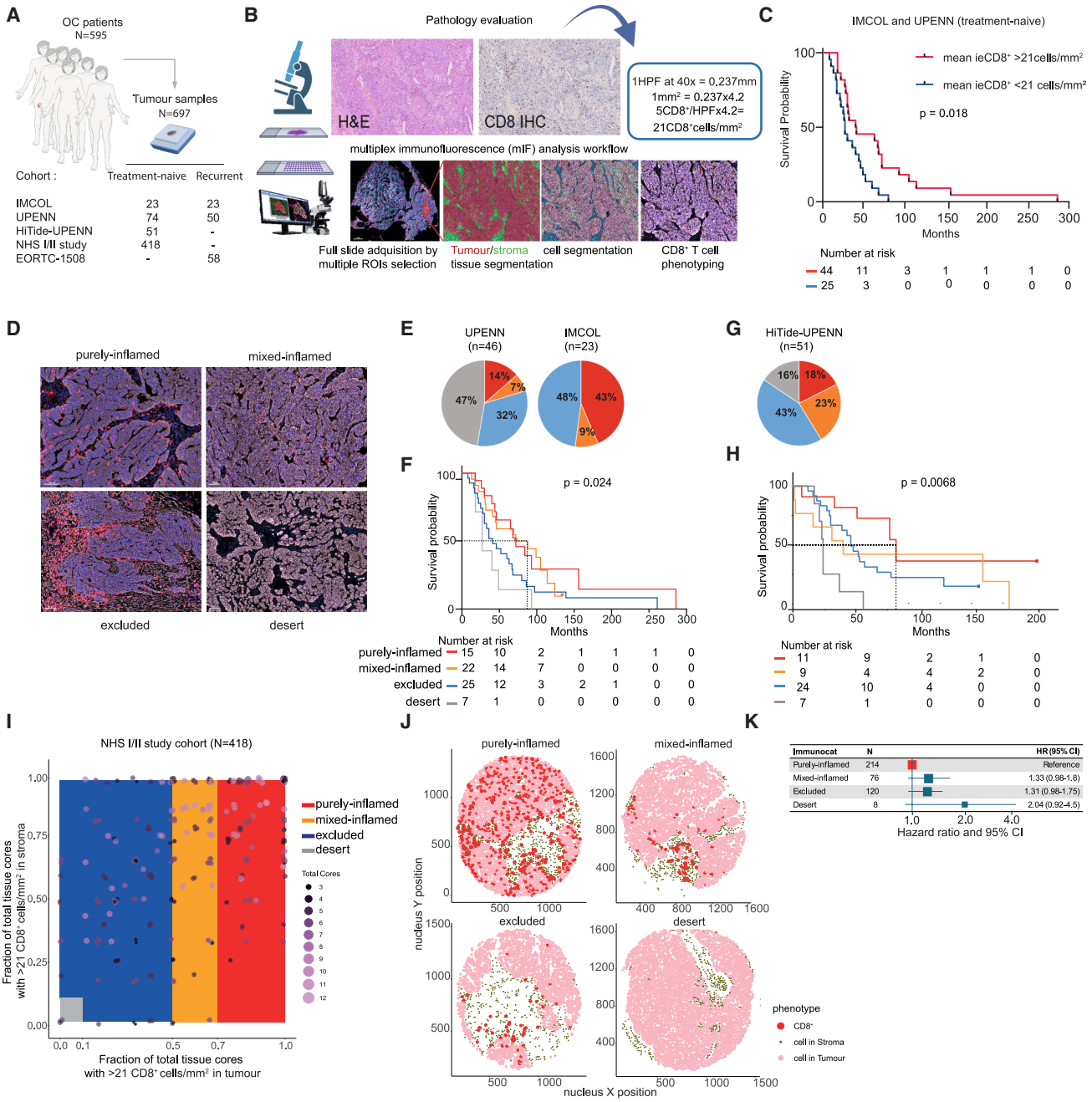

Figure 1. Multiplexed immunofluorescence imaging reveals four different CD8⁺-based OC immune phenotypes which correlate with clinical outcome

(A) Schematic representation of the OC primary-recurrent samples collection coming from five different clinical cohorts.

(B) Schematic of FFPE tissues imaging analysis from IHC to mIF.

(C) Kaplan-Meier curve of overall survival (OS) in the IMCOL and UPENN cohort (treatment-naïve samples only) according to the mIF cut-off of 21CD8⁺/mm².

(D) Representative mIF images of the four immune phenotypes, scale bars, 100 μm.

(E) Pie charts representing the percentage of the four immune categories in the treatment-naïve samples of our training cohorts (UPENN and IMCOL).

(F) Kaplan-Meier curve of OS in the IMCOL and UPENN cohorts according to immune phenotypes.

(G) Pie chart representing the percentage of the four immune-categories in the treatment-naive tumors from the validation cohort HiTide-UPENN.

(H) Kaplan-Meier curve of OS in the HiTide-UPENN cohort according to immune phenotypes.

(I) Schematic representation of our CD8⁺-based immune phenotype algorithm according to the fractions of inflamed ROIs in tumor (*x* axis) and stroma (*y* axis) in the NHS I/II study cohort (*N* = 418).

(J) Reconstructed images of original tumor microarrays (TMAs) of the NHS I/II cohort according to the immune phenotype.

(K) Cox multivariate model of OS in the NHS I/II dataset according to immune category.

Statistical analysis: Log rank test (C,F,H), *p* values < 0.05 considered significant. Also see Figure S1.

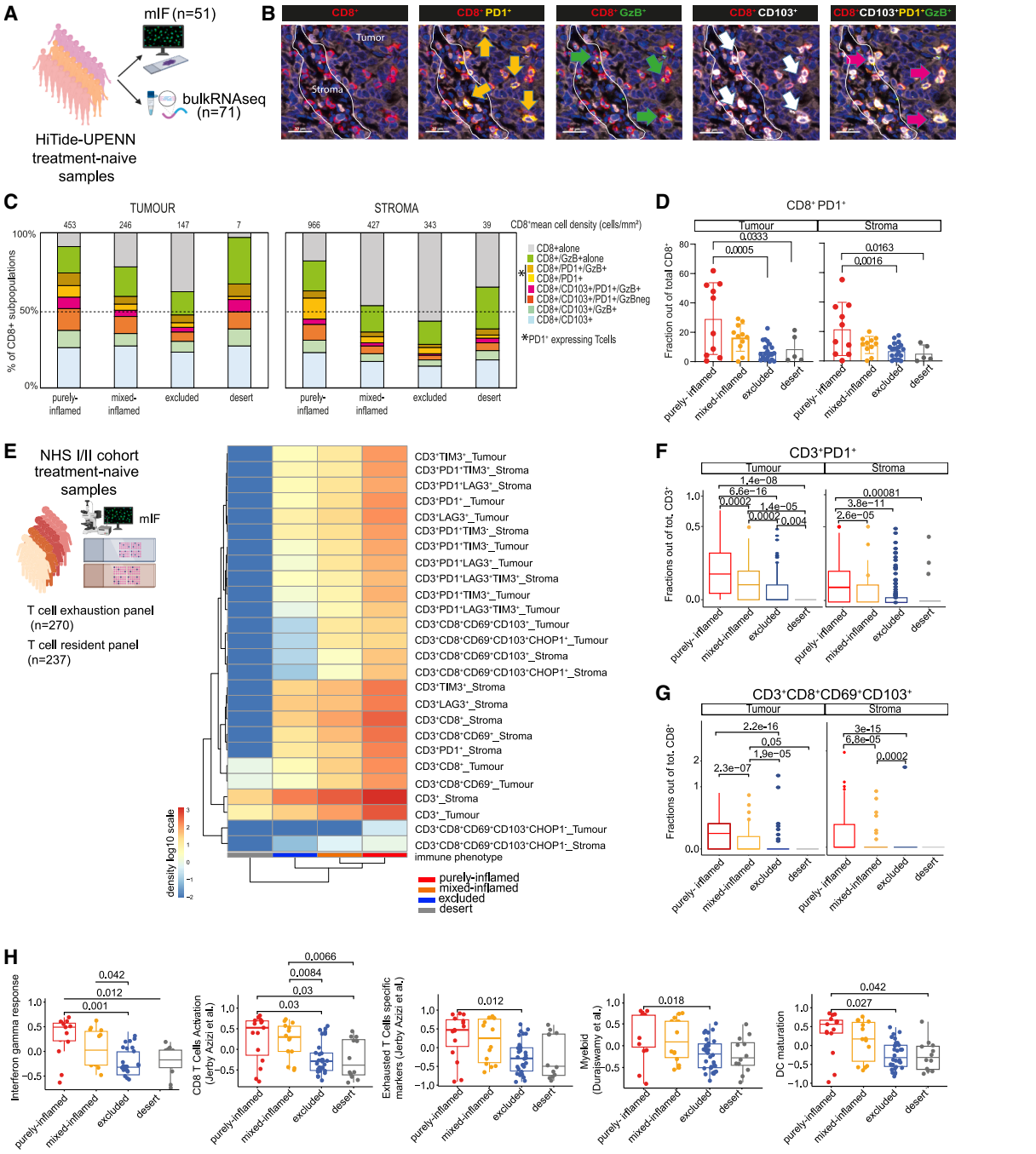

Figure 2. OC immune phenotypes are characterized by distinct TILs and TME states

(A) Schematic representation of the HiTide-UPENN treatment-naive OC cohort (N = 51 FFPE tissues for mIF imaging and N = 71 snap frozen material for bulk RNA).

(B) Example of mIF panel with deconvoluted images for each marker: arrows indicate the TILs subset of interest as labeled in the upper part.

(C) Proportions of T cell subset of interest out of total $CD8^+$ T cell profiled by mIF according to immune phenotypes. Total $CD8^+$ T cell density (cells/mm^2) according to immune phenotypes reported in the upper line.

(D) Proportions of $CD8^+PD1^+$ T cell subset out of total $CD8^+$ T cell profiled by mIF according to immune phenotypes.

(E) Left: schematic representation of the NHS I/II cohort stained by mIF for a T cell exhaustion panel (N = 270) and a T cell resident panel (N = 237). Right: heatmap showing the median cell density (log_{10} scale) of the different T cell subsets clustered according to immune phenotype.

(F and G) Fractions of $CD3^+PD1^+$ and $CD3^+CD8^+CD69^+CD103^+$ T cell subsets identified by mIF according to immune category.

(legend continued on next page)

instability can also positively affect prognosis.[13] To address the association between inflammation, HRD, and outcome in our dataset, we employed copy number and single nucleotide variant (SNV) calls from exome sequencing of primary tumors from 18 patients with OC and further assigned them mutational signature and HRD positivity[28] or by quantifying the levels of mutational signature 3 (SBS3), telomeric allelic imbalance (telomeric AI), large scale transitions (LSTs), loss of heterozygosity (LOH), and ID8/ID9 signatures[29] (Figure S1G). HRD positive OCs (13/18 cases) were significantly associated with chromosomal instability (number of breakpoints/chromosome) (Figure S1H). Also, HRD positivity correlated with better OS (Figure S1I). Importantly, inflamed HRD-positive tumors, as called by our immune classifier, corresponded to long-term survivors and had better outcomes than HRD positive but non-inflamed tumors (excluded and desert) or HRD negative patients (Figure S1J). Our data suggest that long-term survivors are those who carry chromosomal instability due to loss of HR proficiency as well as high and homogeneous CD8 inflammation in tumor epithelium. Thus, integrating genomic alterations[30] and digital immune classification could represent a combined biomarker to improve patient stratification for therapy.[31,32]

OC immune phenotypes are characterized by distinct TILs and myeloid cell states

The significant clinical association of $CD8^+$ immune phenotypes with survival prompted us to investigate deeper their TILs and TME states and potentially explain how $CD8^+$ T cells number and distribution in OC tissues are regulated. To do so, we focused on the HiTide-UPENN cohort (treatment-naive samples, Table S2A) for which both FFPE and snap frozen material was available (Figure 2A). Through mIF staining (Figure 2B and STAR Methods), we observed a significant enrichment in $PD1^+CD8^+$ T cells in purely inflamed tumors, while no differences for $CD103^+CD8^+$or GzB^+CD8^+ T cell proportions were observed across the four immune phenotypes (Figures 2C and 2D). To interrogate more deeply TIL activation and exhaustion states, we analyzed more than 200 treatment-naive OC cases from the NHS I/II cohort for which T cell exhaustion and resident mIF panels were available (Figure 2E and STAR Methods). A striking gradient was observed in the densities of activated, exhausted, and tissue resident $CD8^+$, suggestive of enrichment in antigen specific TILs,[11] between excluded and inflamed OC tissues while those were largely absent in desert OC tumors. Moreover, purely inflamed tumors exhibited the highest densities and proportions of $CD3^+PD1^+$ or $CD3^+CD8^+CD69^+CD103^+$ T cells and other subsets in both the intra-tumoral and stromal compartment (Figures 2E–2G).

To gain more insight on the molecular T cell networks characterizing each immune phenotype, we interrogated bulk RNA sequencing (RNA-seq) data of independent tissue sites from the same patients as aforementioned (STAR Methods). Unsupervised clustering based on Hallmarks Reactome signatures (Figure S2A) revealed that most inflamed tissues segregated together and exhibited higher levels of inflammatory signatures including interferon alpha and gamma response signaling. Indeed, unsupervised clustering based on a collection of published gene signatures capturing more in depth T and myeloid cell activation[16,33–36] (STAR Methods and Table S2B) revealed higher segregation of inflamed tissues and separated them from those assigned as excluded/desert based on corresponding mIF regions (Figure S2B). In a few cases (for example S36), where multiple adjacent tissues were interrogated, we observed a discrepancy in their clustering which is attributed to intrinsic intratumoral heterogeneity (ITH) often observed in OC[12,21,37] (Figures S2A and S2B). Comparative bulk RNA-seq analysis revealed that inflamed tissues exhibited an increase in numerous T cell activation and exhaustion signatures[33–35] (Figure 2H). Interestingly, inflamed tumors also exhibited higher levels of myeloid cell-related antigen presentation signatures, DC maturation,[38] and M1-macrophages[39] (Figure 2E), complement and cytokine signaling[40] denoting that TILs:myeloid cell crosstalk, crucial for T cell engraftment and T cell costimulation.[16] Finally, we observed higher expression of signatures related to cancer progression and resistance to therapy in excluded and desert samples, including epithelial-mesenchymal transition (EMT), matrix remodeling, WNT-beta-catenin signaling, and angiogenesis-related signatures (Figure S2C).[41,42] These associations could explain the observed exclusion of $CD8^+$ T cell from tumor islets and the worse prognosis linked to these immune phenotypes.

In conclusion, we show that OC immune phenotypes exhibit not only different density and spatial $CD8^+$ T cells distribution but also phenotypically divergent TILs and myeloid cell states which could contribute to the observed differential clinical outcomes.

TILs:myeloid crosstalk varies vastly across OC $CD8^+$ immune phenotypes

A mounting body of evidence indicates that the state of terminally exhausted $CD8^+$ TILs may vary depending on their cellular interactions with myeloid cells.[16,43,44] To understand if the enrichment of antigen experienced/exhausted $CD8^+$ TILs in inflamed samples is indeed sustained by the presence of intratumoral myeloid cells, we analyzed treatment-naïve specimens from our two training, whole-slide FFPE, cohorts (Figure 3A; Tables S1A and S1B) by mIF (Figure 3B). We found higher $CD11c^+$ density in purely inflamed samples compared to mixed or excluded cases in the tumor compartment but no differences with desert cases (Figure 3C), suggesting that differential subsets of $CD11c^+$ myeloid cells must reside in inflamed and desert cases which cannot be captured merely by one marker. When analyzing the total infiltration of $CD68^+$ tumor associated macrophages (TAMs) in the UPENN cohort, we indeed observed that these were quasi-universally present except for five purely inflamed samples where they were completely absent (Figure 3D). To characterize the states of the myeloid compartment in our OC immune phenotypes, we analyzed 246 OC

(H) Selected significant differential pathways from bulk RNA sequencing analysis in the HiTide-UPENN cohort among the four immune categories (full list in Table S2).

Data shown as mean ± SD in (C, D, F, G, and H). Statistical analysis: unpaired, two-tailed Wilcoxon-rank test (C, D, F, and G), corrected by Bonferroni correction (H). p values < 0.05 considered significant. Also see Figure S2.

CellPress
OPEN ACCESS

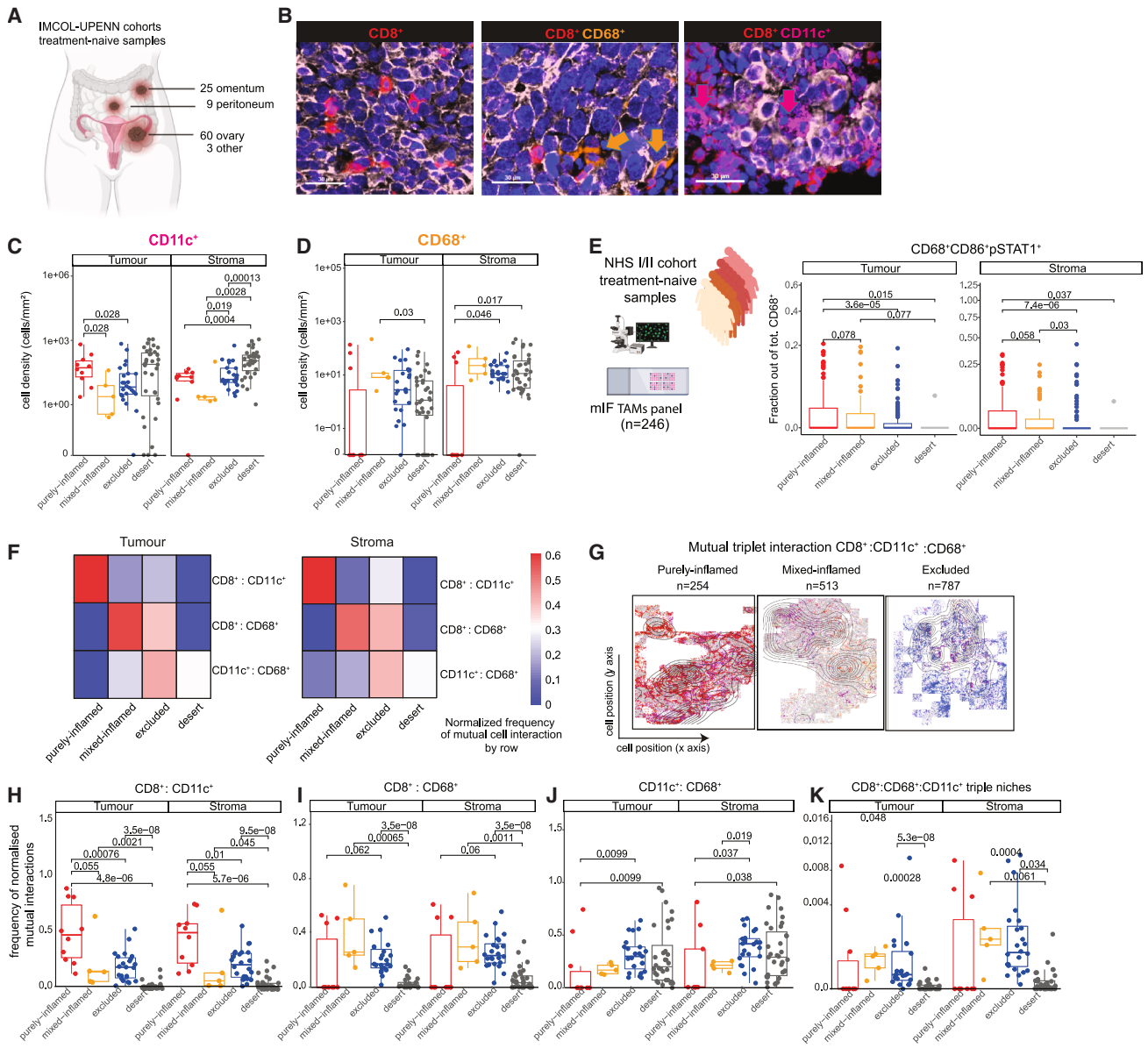

Figure 3. TILs: myeloid crosstalk varies vastly across OC CD8⁺ immune phenotypes in treatment-naive tumors

(A) Schematic representation of the tissue site of origin for samples harvested at primary surgery (treatment-naïve tumors for the UPENN and IMCOL cohorts merged).

(B) Example of the mIF panel with deconvoluted images for each marker: the immune population of interest is indicated by arrows and color-coded as labeled in the upper part.

(C and D) Cell density (cells/mm^2, $\log_{10}$ scale) profiled by mIF for CD11c$^+$ and CD68$^+$ according to immune phenotypes in the UPENN cohort.

(E) Left: schematic representation of the NHS I/II cohort (treatment naive samples) stained by mIF (N = 246). Right: fraction of the CD68$^+$CD86$^+$pSTAT1$^+$ subset identified by mIF according to immune category.

(F) Heatmaps showing the normalized frequency of mutual cell interaction at a 20 μm neighboring radii in the UPENN cohort. Immune cell population interaction of interest in lines and immune categories as columns. Color-code scale bar showing the normalized frequency by row.

(G) Digital tissue reconstruction showing Kernel density estimation of the frequency of triple mutual interaction CD8$^+$:CD68$^+$:CD11c$^+$ according to immune phenotypes.

(H–K) Frequency of mutual interaction between the indicated cell types according to immune phenotypes.

Data shown as mean ± SD in (C–E and H–K). Statistical analysis: unpaired, two-tailed Wilcoxon-rank test (C–E and H–K). p values < 0.05 considered significant. Also see Figure S3.

primary cases from the NHS I/II cohort with a TAM mIF panel (Figure 3E and STAR Methods). As previously suggested by our bulk RNA-seq analysis (Figure 2E), inflamed tumors harbored the highest proportions of activated TAMs or myeloid cells with protein overexpression of CD86 and pSTAT1 (Figure 3E) demonstrating that this subgroup harbors also key macrophage subtypes linked to anti-tumor immune responses.

To gain more insight into differential TME architectures, we interrogated cellular crosstalk between $CD8^+$ TILs and myeloid populations. Our work and others have recently shown the existence of intratumoral niches where critical T cell-DC interactions occur.[16,45,46] We derived a mutual cell-to-cell interaction neighborhood which calculates the normalized frequency of cell-to-cell interactions among two[44] or more cell types (Figures 3E, 3G, and S3A and STAR Methods). We showed that purely inflamed samples exhibited significantly higher $CD8^+$:$CD11c^+$ interactions in both the tumor and stromal compartment compared to all other immune phenotypes (Figures 3F–3H). Instead, mixed-inflamed and excluded tumors harbored higher $CD8^+$:$CD68^+$interactions (Figure 3I). Although cell frequencies and their mutual interaction are interdependent by design, we found that $CD8^+$:$CD11c^+$ cells interaction separated purely inflamed samples from other immune phenotypes significantly better than their respective minimal cell frequency (Figure 3C). Of note, we also observed that excluded and desert tumors exhibited increased $CD11c^+$:$CD68^+$ (or homotypic myeloid) interactions (Figure 3J) and wondered if those myeloid niches could also harbor $CD8^+$ TILs. We thus computed the occurrence of triplet niches *in situ* (STAR Methods). Mixed-inflamed and excluded samples had higher levels of triplets populated by $CD8^+$:$CD11c^+$:$CD68^+$ in the tumor and even more in the stroma (Figure 3K). This led us to hypothesize that some TAM states could interfere with productive $CD8^+$:$CD11c^+$ interactions thus impairing T cell co-stimulation. When extending our analyses to include T cells with PD1 or myeloid cells with PD-L1 expression, we confirmed an enrichment of $CD8^+PD1^+$ cells interacting with $CD11c^+$ cells expressing or not PD-L1 in purely inflamed, suggesting the relevance of PD1/PDL1 axis in this OC subgroup (Figure S3B). Importantly, patients with primary tumors enriched in myeloid niches marked by PD-L1 expression had a significantly worse progression-free survival (PFS) compared to those with low $CD11c^+$:$CD68^+PD\text{-}L1^+$ niches (Figures S3D and S3E).

These results highlight the differential $CD8^+$: myeloid crosstalk established among OC immune phenotypes. The subset of purely inflamed OC is selectively enriched for $CD8^+$:$CD11c^+$ niches recently shown to be essential for response to ICIs[16,46,47] and adoptive T cell therapy.[44] They also suggest that the type of myeloid cells infiltrating tumors could be further regulating T cell distribution in the TME.[48]

HRD status and TILs:myeloid crosstalk define OC immune phenotype evolution and architecture at recurrence

We then sought to decipher the evolution of immune phenotypes upon standard-of-care CTX and recurrence taking advantage of our patient-matched tumor tissues harvested at secondary cytoreductive surgery (Figure 4A; Tables S1A and S1B). We applied our immune classification in recurrent OCs tissues and observed that the trajectory and evolution of immune phenotypes was highly dynamic (Figure 4B). Nevertheless, purely inflamed OC retained their homogenous $CD8^+$ inflammation whereas most desert carcinomas remained desert upon recurrence, suggesting that re-emerging tumors could reconstitute their $CD8^+$ spatial distribution and, by extension, their TME.

Interestingly, when tracking the evolution of immune phenotypes according to HRD status, we showed that whereas HRP tumors largely spread across different immune phenotypes and toward an excluded or desert phenotype, most recurrent BRCA/HRD retained or even evolved toward an inflamed state (Figures 4C–4E). Importantly the evolution toward an inflamed phenotype at recurrence was associated with a benefit in OS (Figure 4F).

When interrogating TILs:myeloid cell neighborhoods we saw that recurrent purely inflamed tumors retained the highest frequency of $CD8^+$:$CD11c^+$ interactions (Figures 4G and 4H). Mixed-inflamed cases were enriched in both $CD8^+$:$CD11c^+$ and $CD8^+$:$CD68^+$ interactions (Figure 4I). Finally, recurrent excluded tumors were mostly enriched by $CD8^+$:$CD68^+$ (Figure 4I) and triplet ($CD8^+$:$CD11c^+$:$CD68^+$) niches similarly to primary OC (Figure S3F).

Notably, when assessing niches evolution according to HRD status in our cohorts, we observed that while HRD cases significantly increment $CD8^+$:$CD11c^+$ niches at recurrence in both the tumor and stroma compartment, being higher than HRP cases (Figure 4J). On the contrary, HRP recurrent OCs showed higher $CD8^+$:$CD68^+$ niches (Figure 4K) and homotypic interactions (Figure S3G).

We then investigated the role of myeloid-T cell niches for response to ICIs in recurrent platinum-resistant OC samples collected before treatment initiation from patients enrolled in the EORTC-1508-GCG phase II clinical trial[49] (Figure 4L and STAR Methods). By computing mutual TILs:myeloid cell interactions as aforementioned, we showed that responders to combinatorial ICI therapy exhibited higher $CD8^+$:$CD11c^+$ and $CD8^+$ $PD\text{-}1^+$:$CD11c^+$ niches compared to non-responders but no differences in $CD8^+$:$CD68^+$ niches, thus validating the relevance of T cell: DC networks for response to ICIs in the context of heavily pre-treated OC disease.

Despite the limitation of having patient-matched but not site-matched samples, our analyses revealed that immune cell dynamics are affected by disease progression, but the key TME players and interactions are rather stable at recurrence in OC immune phenotypes. Purely inflamed tumors maintain $CD8^+$:DC crosstalk, while mixed inflamed and excluded OC exhibit higher TILs:TAMs and homotypic myeloid interactions, thus suggesting a faster evolution toward an immune-resistant phenotype with rare tumor-reactive resident TILs able to abrogate malignant progression.[11,50] Our data also suggest that HRD mutational status could potentially determine tumor immune phenotype evolution and thus warrants the further investigation given in the following text.

Temporal heterogeneity of T:myeloid cell inflammation in recurrent mouse OC models

To further disentangle the molecular mechanisms underlying TIL infiltration and TME orchestration, we set out to build orthotopic mouse OC models with defined HRD status which resemble primary and recurrent human OCs as well as their respective TMEs.

CellPress
OPEN ACCESS

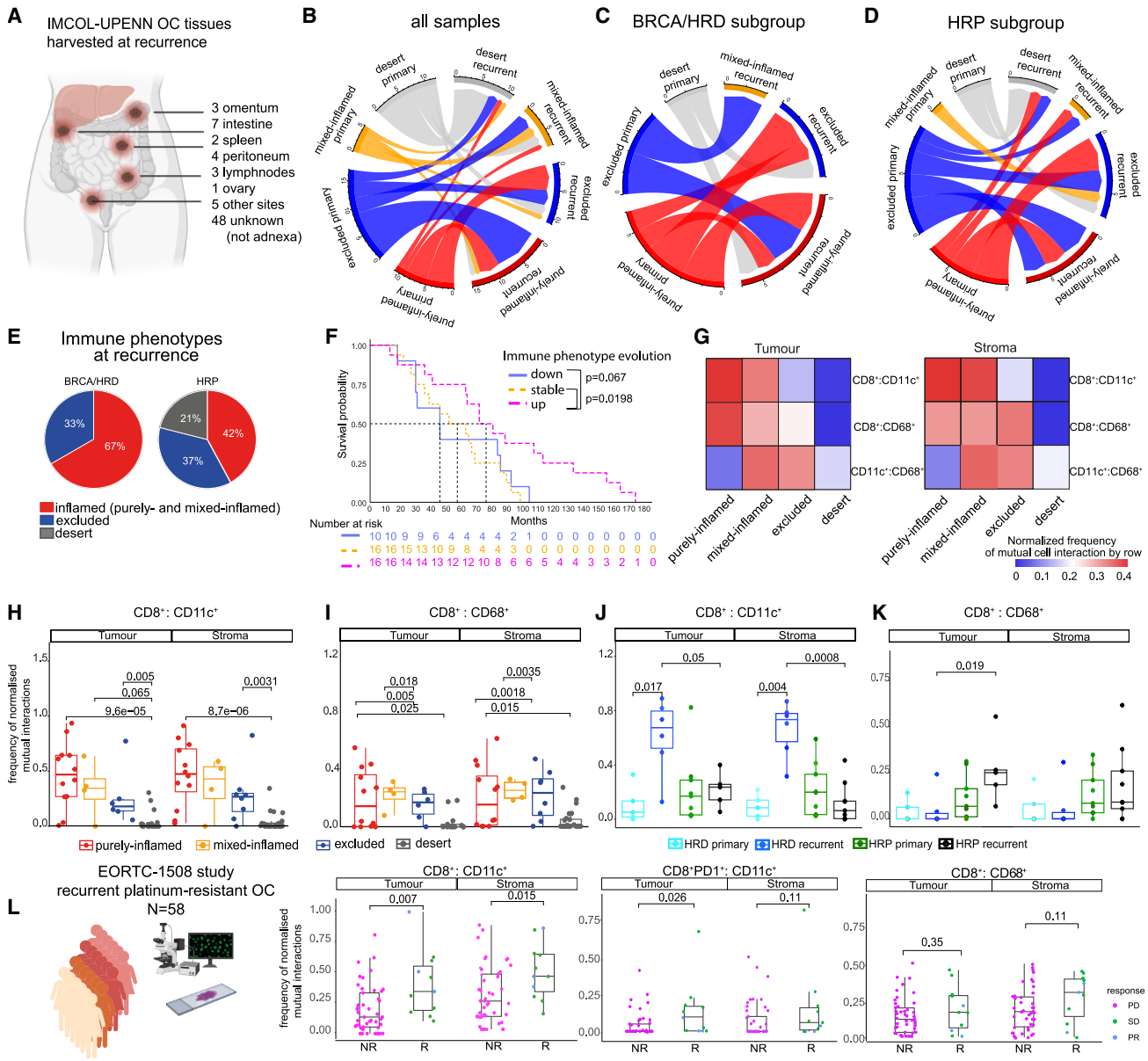

Figure 4. Myeloid crosstalk at recurrence define the evolution of OC TME architecture together with HRD status

(A) Schematic representation of the tissue site of origin for samples harvested at recurrence (UPENN and IMCOL recurrent tumors, cohorts merged).

(B–D) The evolution of immune phenotypes for patient-matched samples (UPENN and IMCOL cohorts merged) in the BRCA/HRD and HRP subgroups separately.

(E) The percentage of the immune phenotypes at recurrence in the BRCA/HRD and HRP subgroups.

(F) Kaplan-Meier curves of OS according to immune phenotype evolution at recurrence.

(G) Heatmaps showing the normalized frequency of mutual interaction between cell types at a 20 μm neighboring radii at recurrence for UPENN cohort. Immune cell population interaction of interest in lines and immune categories as columns. Color-code scale bar showing the normalized frequency by each row.

(H and I) Frequency of mutual interaction between the indicated cell types according to immune phenotypes at recurrence.

(J and K) Frequency of mutual interaction between the indicated cell types according to HRD status at primary and recurrence (L) Left: schematic representation of the EORTC-1508-GCG cohort analyzed by mIF; right: frequency of mutual interaction between the indicated cell types in responders (Rs) and non-responders (NRs) according to RECIST v.1.1 criteria.

Data shown as mean ± SD in (H–L). Statistical analysis: Log rank test (F), unpaired, two-tailed Wilcoxon-rank test (C–E and H–K). *p* values < 0.05 considered significant.

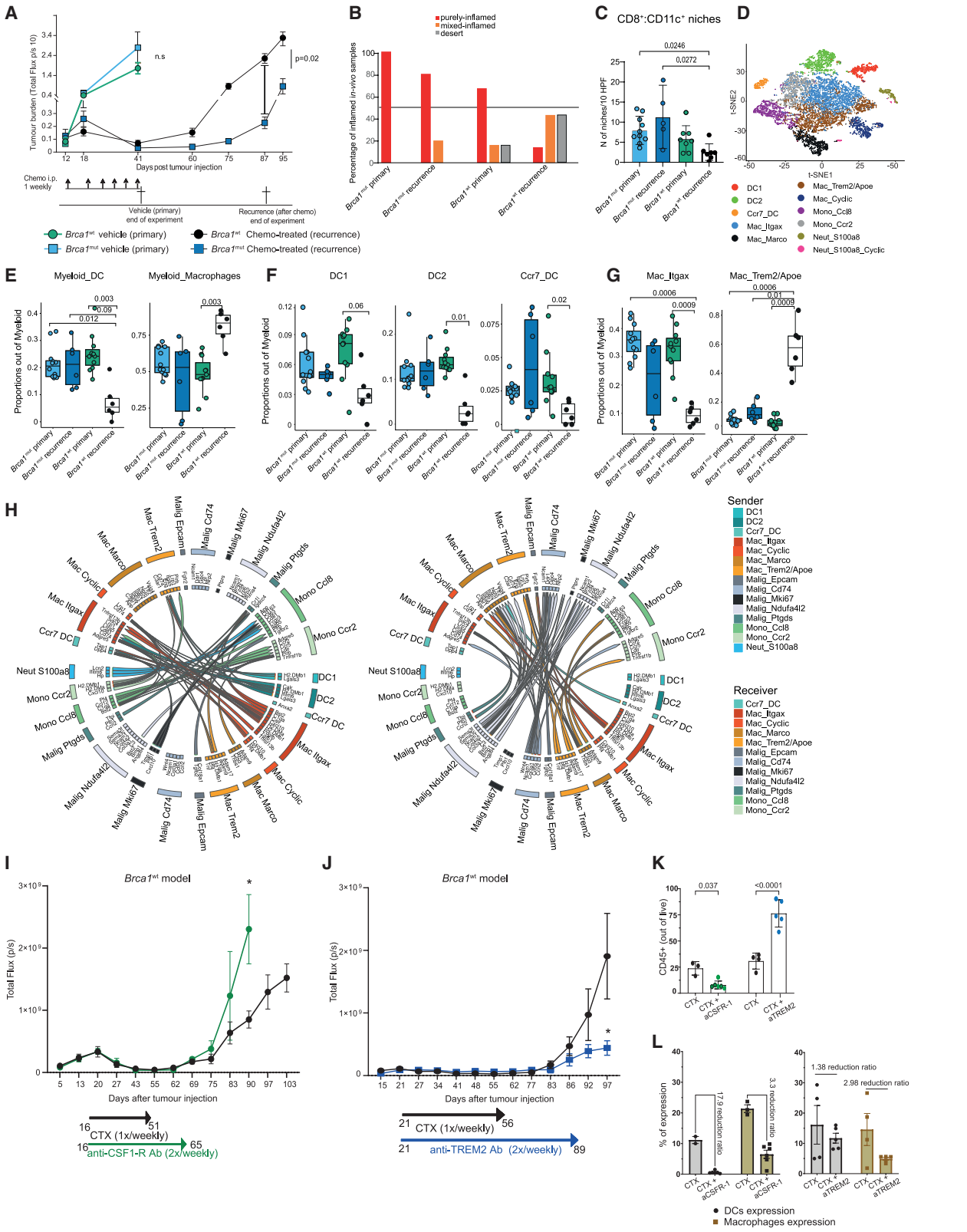

(legend on next page)

We employed the syngeneic ID8 cell lines knocked out for *Trp53* and *Brca1* genes[51,52] (STAR Methods) and further engineered to overexpress luciferase.[36] Mice were orthotopically implanted with *Trp53*$^{-/-}$ *Brca1*$^{-/-}$ (hereby referred as *Brca1*^{mut}) or *Trp53*$^{-/-}$ *Brca1*$^{+/+}$ (or *Brca1*^{wt}) ID8 tumor cells and treated weekly with dual CTX (carboplatin/paclitaxel) for 6 cycles, mimicking first line clinical standard-of-care. Bioluminescence abdominal quantification revealed partial or even complete tumor regression upon CTX in mice, before they all eventually recurred with *Brca1*^{mut} having a slower relapse kinetic than *Brca1*^{wt} (Figures 5A and S4A).

To immune-classify and study TILs:DCs crosstalk in our primary and recurrent mouse models, we performed a triple IHC staining for CD8$^+$, CD11c$^+$, and panCK$^+$ cells in mouse tumor tissues. *Brca1*^{mut} displayed higher levels of CD8$^+$ and CD11c$^+$ densities at baseline and maintained them at recurrence while strikingly *Brca1*^{wt} lost both CD8$^+$ TILs and CD11c$^+$ (Figure S4B). Only *Brca1*^{mut} remained homogenously inflamed at recurrence with concomitant higher CD8$^+$:CD11c$^+$ niches while recurrent *Brca1*^{wt} tumors evolved mainly into desert phenotypes with a global depletion of CD8$^+$:CD11c$^+$ niches (Figures 5B and 5C). This observation was validated in our human dataset showing that indeed, only human HRD cases maintained CD8$^+$ and CD11c$^+$ infiltration and niches upon recurrence to first-line CTX (Figures 4J and S4C).

The aforementioned findings indicated that *Brca1*^{mut} tumors recapitulate the HRD purely inflamed cases observed in the human dataset characterized by homogenous CD8$^+$ TIL infiltration and high number of TILs:APC interactions. On the contrary, *Brca1*^{wt} (mainly desert at recurrence) may reflect CTX-resistant tumors where an immune-suppressive TME with loss of TILs and DCs develops upon progression.[53]

Thus, we further dissected and compared the evolution of the TME in our primary-recurrent OC models by scRNA-seq. We analyzed 39,752 cells distributed into 17 major clusters (STAR Methods) and identified six major cell classes (Figures S4D and S4E) and 14 subclasses (Figure S4F). We validated by scRNA-seq that purely inflamed mouse OC tissues exhibited higher proportions of T cells and myeloid DC cells compared to mixed-inflamed and desert samples while mixed and desert samples were enriched in myeloid macrophages and malignant subsets (Figures S4G and S4H). While we could observe a global loss of T cells in *Brca1*^{wt} and their maintenance in *Brca1*^{mut} tumors (Figure S4B), more changes appeared in their composition at recurrence. The CD8 and CD4 naive-like, effector memory, and exhausted TIL subsets remained unaltered (Figure S5A), while the CD4-resting state increased in recurrent *Brca1*^{mut} tumors (Figure S5B). In addition, *Brca1*^{mut} recurrent tumors maintained a higher type-I interferon CD8 TIL state which was lost in *Brca1*^{wt} and increased the frequency of *Hsp*^{high} CD8 TIL state (Figure S5C). The NK or NK-like cells represented a small compartment among all T cells and were annotated in three subsets, namely NK cells and CD8 or CD4 NK-like T cells (Figure S5A). When comparing their proportions at primary or recurrent stages, we observed that *Brca1*^{mut} tumors retained NK cell levels at recurrence. While the majority of recurrent *Brca1*^{wt} tumors lost NK cells, there was a vast variability in NK cell levels at recurrence (Figure S5D).

To further understand how the stromal compartment evolves during ovarian cancer recurrence, we compared changes of endothelial and fibroblast populations at baseline and recurrence. In both tumor models, we observed a striking increase of endothelial cells after CTX, suggesting that cancer progression drives angiogenesis (Figures S5E and S5F). In addition, recurrent *Brca1*^{mut} reshaped their CAF composition by significantly reducing the clusterin^{high} (*Clu*^{high})-CAFs state which modulate the adjacent TME via transforming growth factor β (TGFβ) signaling[54] and by increasing the inflammatory *Gsn*^{high}-CAFs cluster (Figure S5G), reported to overexpress multiple pathways involving *Ptgis* (prostaglandin I2 synthase) and complement activation through C3 and CFD[55] (Table S3B).

ApoE/Trem2 signaling drive immunosuppressive TAM networks in recurrent *Brca1*^{wt} tumors and its blockade *in vivo* delays OC recurrence

Having described a clear interplay between myeloid cells and TILs in our human dataset, we investigated the evolution of myeloid cell subtypes in our mouse models (Figure 5D). Comparative analysis showed a drastic decrease of DCs affecting all subsets (cDC1, cDC2,and CCR7$^+$DC) in recurrent *Brca1*^{wt} tumors (Figures 5E and 5F). This was counterbalanced by a global increase in macrophages and specifically by *Trem2/ApoE* TAM state[56,57] (Figure 5G), characterized among others by stress-induced senescence and TNFR1-driven nuclear factor kappa B (NF-kB) signaling and involved in high-density lipoprotein (HDL) metabolism[58,59] (Figure S5H; Table S4E). A clear dichotomy was observed between our two models at recurrence where *Itgax*-TAMs overexpressing *Cxcl9*, *Cxcl16*, and *Il1b* were

Figure 5. *Brca1*^{wt} tumors lose TILs:APC interactions and upregulate immunosuppressive TAMs at recurrence which can be target *in vivo* to delay OC recurrence

(A) Tumor growth kinetics of ID8*Luc Trp53*$^{-/-}$ *Brca1*^{wt} and *Brca1*^{mut} during treatment in the control (vehicle or primary) or chemotherapy group (CTX, recurrence) (n = 6–7 mice per group).

(B) Percentages of immune phenotypes in the *Brca1*^{wt} and *Brca1*^{mut} tumors at primary and recurrence.

(C) CD8$^+$:CD11c$^+$ niches assessed by IHC between *Brca1*^{mut} and *Brca1*^{wt} tumors at baseline and recurrence.

(D) t-SNE map of the *in-vivo* single-cell transcriptomic data displaying the identified myeloid clusters.

(E–G) Proportion of the indicated myeloid classes and subclasses between *Brca1*^{mut} and *Brca1*^{wt} tumors at baseline and at recurrence.

(H) Circos plot of interactome analysis by MultiNicheNet displaying finer subclasses interaction within the top 5 cell type interactions between *Brca1*^{mut} and *Brca1*^{wt} recurrent tumors.

(I and J) Tumor growth kinetics of ID8*Luc Trp53*$^{-/-}$ *Brca1*^{wt} during treatment with chemotherapy (CTX) and CTX + anti-CSFR1 (left) or CTX + anti-TREM2 Ab (right) (*n* = 6–7 mice per group).

(K and L) *ex vivo* FACS data comparing the percentage of CD45$^+$ cells and the reduction ratio of DC and macrophages in previous experiment (I and J).

Statistical analysis: two-way ANOVA (A, I, and J), unpaired, two-tailed Wilcoxon-rank test (E–G and K and L). *p* values < 0.05 considered significant. Also see Figures S4–S7.

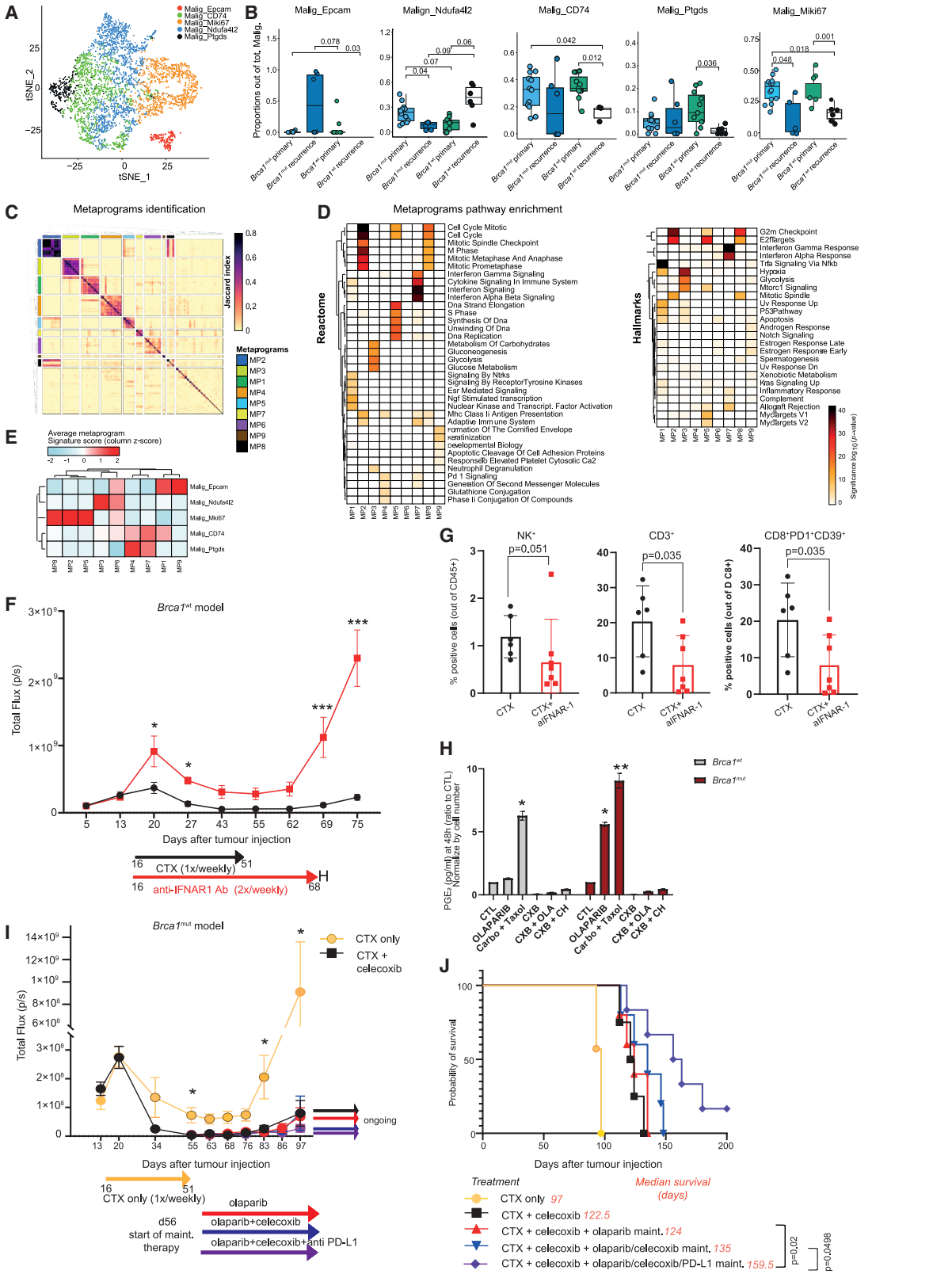

Figure 6. Tumor-intrinsic mechanism of resistance to CTX of *Brca1*^{mut} tumors include the PGE$_2$-axis upregulation

(A) t-SNE map of the *in-vivo* single-cell transcriptomic data displaying the identified malignant clusters.

(B) Proportion of the indicated malignant subclasses between *Brca1*^{mut} and *Brca1*^{wt} tumors at baseline and at recurrence.

(legend continued on next page)

completely lost at recurrence in *Brca1*^{wt} tumors while they were maintained, together with all the DC subsets, in *Brca1*^{mut} cancers (Figures 5F and 5G). In line with these results, we also showed, in a subset of patients from the IMCOL-UPENN cohorts, that human HRD tumors exhibited higher level of CXCL9^{+} CD68^{+} TAMs compared to HRP ones, and that CXCL9^{+} TAM infiltration correlated with CD8^{+} TIL levels (Figure S5I).

The aforementioned findings prompted us to predict the signaling networks and infer the cellular crosstalk established in the TMEs of these temporally divergent tumor immune phenotypes. By applying MultiNicheNet,[60] we revealed highly divergent regulatory networks at recurrence between our models (Figure S6A). While *Brca1*^{mut} displayed a myeloid:T cell network sustaining antigen presentation and chemokine activation, a plethora of inhibitory macrophages-malignant and homotypic myeloid cell signaling and interactions dominated *Brca1*^{wt} tumors with downregulation of antigen presentation. To increase resolution in the interactome, we next focused on the top five cell-type ligand-receptor interactions of each recurrent tumor model. Again, we found that DCs:B cells:CD4 T cells interactions were maintained in *Brca1*^{mut} upon recurrence and lost in *Brca1*^{wt} (Figure S6B; Tables S4A and S4B). These were sustained by the highly important *Cxcl9/Cxcl10-Cxcr3* axis for OC[40] and provide TILs co-stimulation through CD28.[16,40] On the contrary, *Brca1*^{wt} tumors were dominated by homotypic myeloid-cell crosstalk including macrophages:DCs predicted to interact predominantly through *Trem2/Apoe*^{high} TAMs and mediated by *Tgfb1*, *Fn1*, *App*, and *Thbs1* ligands associated with EMT, invasiveness, and metastatic spread[61,62] (Figure 5H).

Our systematic analyses highlighted the abundant enrichment of immunosuppressive TAMs in HRP tumors and their marked post-CTX treatment increase, which may be a key contributor to their recurrence. This was consistent with our observations in HRP patients' specimens (Figure S5H) and prompted us to test the hypothesis that directly targeting the macrophage compartment in combination with CTX would delay recurrence in HRP tumors. We utilized our *Brca1*^{wt} model described previously and treated mice with standard-of-care dual CTX in combination with antibodies targeting the macrophage colony stimulating factor 1 receptor (CSF-1R) or specifically the TREM2 receptor (Figures 5I and 5J and STAR Methods). Surprisingly, we showed that CSF-1R blockade resulted in a faster recurrence of *Brca1*^{wt} ovarian cancer *in vivo* (Figure 5I). *Ex vivo* flow cytometry (FACS) analysis of recurrent *Brca1*^{wt} tumors revealed a drastic reduction of MHC-II^{+} DCs, total macrophages and M2-like TAMs in the combination group compared to CTX alone, both in the tumor and in the ascitic fluid (Figure S7A), pointing out to a non-selective myeloid depletion in the TME. Instead, TREM2 neutralization in the same model, showed a significant delay in the recurrence *of Brca1*^{wt} ovarian cancers after CTX (Figure 5J). *Ex vivo* FACS analysis of *Brca1*^{wt} recurrent tumors revealed a significant increase in the tumor-infiltrating CD45^{+} leukocytes for the TREM2-treated group and a significant decrease for the CSF-1R treated one (Figure 5K) which correlated inversely with tumor volumes (Figure S7B). Interestingly, *in vivo* TREM2 blockade spared DCs (Figures 5L and S7C) and promoted a slight decrease in the myeloid compartment, with a significant reduction in M2-like macrophages (Figure S7C). These results were in line with the expression levels of *Csfr-1* and *Trem2* in the myeloid compartment of our *in vivo* models. *Csfr-1* was broadly detected in all myeloid states including neutrophils and the DC2 cluster. However, *Trem2* was found overexpressed in *Trem2*$^{+}$ TAMs and detected also in monocytes and other TAMs states but not in DCs or neutrophils (Figure S7D).

Our findings demonstrated that *Brca1*^{mut} retain their tumor immune phenotype due to immunogenic malignant and immune stimulatory myeloid cell subsets. On the contrary, *Brca1*^{wt} (mainly desert at recurrence) establish a TIL-excluding TME due to the loss of activated DCs. In addition, phenocopying tumor progression of immune excluded OC; they reveal upregulation of inhibitory *Trem2/Apoe*^{high} TAMs subsets, potentially recruited by immune evasive *Nduf4l2/Galectin3*^{high} malignant states. Specific TME myeloid targeting with anti-TREM2 neutralizing Ab enhanced the effects of first-line CTX in *Brca1*^{wt} mouse models.

Malignant cell state evolution during OC recurrence

We then focused on the malignant compartment of our models where we identified five different malignant subsets (Figure 6A) and observed divergent evolution at recurrence. *Brca1*^{mut} primary tumors were dominated by malignant cell states such as *Epcam*^{high}, *CD74*^{high}, and *Ptgds*^{high} clusters (Figure 6B; Table S3A) with overexpression of fibroblast grow factor receptor (FGFR) signaling pathways but also antigen processing/presentation genes (MHC class II [*H2-Eb1*, *H2-Ab1*, and *H2-Aa*], *Cd74*, and *Cd86*). *Ptgds*^{high} cluster was also characterized by prostanoid and eicosanoid-associated metabolic signatures and increased specifically after CTX and tumor progression (Figure 6B). Recurrent *Brca1*^{mut} also maintained a highly proliferating *Mki67*^{high} tumor cell state (Figure 6B) with overexpression of genes such as *Hmgb2* and senescence-associated secretory phenotype (SASP).[63] However, recurrent *Brca1*^{wt} significantly lost the *CD74*^{high}, *Mki67*^{high} and *Ptgds*^{high} malignant cell states and were largely repopulated by the immunosuppressive *Nduf4l2*^{high} compartment overexpressing *Lgals1*[64] (Figure 6B;

(C) Heatmap displaying gene non-negative matrix factorization (NMF) and the nine metaprograms (MPs) identified in the malignant compartment.
(D) Pathway enrichment analysis for each MP using both the Hallmarks and the Reactome pathway collections.
(E) Heatmap showing signature scores (*Z* score) for each MPs in each malignant subpopulation.
(F) Tumor growth kinetics of ID8*Luc Trp53*$^{-/-}$ *Brca1*^{wt} during treatment with chemotherapy (CTX) and CTX + anti-IFNAR1 Ab (n = 6–7 mice per group).
(G) FACS data analysis from *in-vivo* experiment in (F).
(H) PGE_2 expressed by *Brca1*^{wt} and *Brca1*^{mut} cell lines assessed by ELISA at the indicated time point and according to the labeled conditions.
(I) Tumor growth kinetics of ID8*Luc Trp53*$^{-/-}$ *Brca1*^{mut} during treatment with chemotherapy (CTX) and CTX + celecoxib (n = 6–7 mice per group).
(J) Survival curve from *in-vivo* experiment in panel I according to the different maintenance treatment groups.
Statistical analysis: unpaired, two-tailed Wilcoxon-rank test (B and G), two-way ANOVA (A and I), Log rank test (J); p values < 0.05 considered significant. Also see Figure S8.

Table S3A). To further interpret the malignant subsets, we carried out meta-programs (MPs) identification[65] detecting nine different MPs (Figure 6C and STAR Methods). Then, we conducted pathway enrichment analysis for each MP using both the hallmarks and the reactome pathway collections (Figure 6D) and computed the signature scores of these MPs in our malignant subtypes (Figure 6E). For instance, we could observe that MP2-5-8 are associated with cell cycle, MP7 is associated with interferon signaling and antigen presentation, and MP3 with glucose metabolism (Figures 6D and 6E). Interestingly, the *CD74*^{high} and *Ptgds*^{high} malignant cell states highly present in *Brca1*^{mut} models (and lost in recurrent *Brca1*^{wt} tumors) showed enrichment for the MP7 described previously as well as for MP4 characterized by PD1 and glutathione conjugation signaling (Figures 6D and 6E).

Our data on the malignant compartment evolution may explain why *Brca1*^{mut} tumors remain immunogenic at recurrence and therefore maintain their TILs:DCs niches but can still evade immune destruction through FGFR[66] and COX-driven prostanoid signaling.[67] In contrast, *Brca1*^{wt} tumors are highly reshaped during tumor progression. They emerge into new immune evading and suppressive malignant states with *Nduf4l2* characterized by a highly glycolytic MP and *Galectin3* overexpression.[64,68,69] These results may explain the observed loss of T cells and stimulatory APCs which indeed leads to faster progression in *Brca1*^{wt} tumors as observed in end-stage human OC.[13]

Finally, to further dissect the tumor-intrinsic mechanism by which *Brca1*^{mut} tumors retain immunogenicity at recurrence, we performed copy-number alteration inferences in our scRNA-seq data of malignant cells by inferCNV analysis[70,71] (STAR Methods). Our data pointed to differences in inferred CNVs between the *Brca1*^{mut} and *Brca1*^{wt} primary tumors, such as copy-number losses and gains in chromosomes 2 and 3 (Figure S8A). Importantly, we showed that while overall CNVs are replicated in both models at recurrence (Figure S8A) in line with recent observations,[13,72] recurrent *Brca1*^{mut} tumors showed a significant increase in inferCNVs (Figure S8B) in association with a reestablishment of their immune landscape. Furthermore, we could observe that the *Epcam*^{high} cluster, predominant in recurrent *Brca1*^{mut} tumors had the most variable CNVs patterns (Figure S8C).

These results highlight highly divergent evolutions in the malignant landscape of HRD and HRP recurrent tumors and could further explain the divergency observed in the temporal tumor immune phenotype evolution of human OC. In summary, recurrent *Brca1*^{mut} tumors retain an immunogenic malignant compartment in association with higher genomic instability while *Brca1*^{wt} tumors evolve into immune evasive malignant states, thus validating that combinations of HRD alterations and differential immune responses contribute to long-term survival in OC (Figure S1J).

Tumor-intrinsic vulnerabilities and mechanisms of OC recurrence

Our transcriptional profiling of malignant cell states suggest that primary tumors retain a metaprogram (MP7) associated with interferon signaling and depending on the HRD status these immunogenic cell states may be reconstructed or lost post CTX and recurrence.

Therefore, we questioned if the interferon signaling axis constitutes a prerequisite for response to dual CTX. To this end, we treated mice bearing *Brca1*^{wt} OC tumors with the usual CTX dual regimen alone or in combination with an antibody blocking the IFN alpha receptor subunit 1 (IFNAR1) (Figure 6F and STAR Methods). Negating type-I IFN TME signaling from treatment onset markedly reduced the therapeutic benefit conferred by CTX and caused an acceleration of OC recurrence (Figure 6F). Furthermore, IFNAR1 blockade marked a decrease in tumor infiltrating NK, T cell (CD3^{+}) and activated exhausted CD8^{+} T cell (Figure 6G) while no significant changes were observed in the myeloid compartment (Figure S8D). To further confirm these findings, we blocked IFNAR1 in the *Brca1*^{mut} model and consistently showed an abrogation of tumor control exerted by CTX control (Figure S8E). Hence, type-I IFN signaling represents a crucial driver for the anti-cancerous effects of CTX.[73]

Our data on the malignant compartment evolution also explained why *Brca1*^{mut} tumors remain immunogenic and inflamed at recurrence but can still evade immune destruction through tumor-intrinsic COX-driven prostanoid signaling[67] (Figure S8F) recently associated with disruption of TILs functionality and ferroptosis.[74] First, we studied the production of PGE_2 by cancer cells as a product of COX-driven prostanoid signaling. Interestingly, we saw that baseline PGE_2 production was significantly upregulated by dual CTX in both *Brca1*^{wt} and *Brca1*^{mut} cell lines (Figures 6H and S8G). Importantly, PARP inhibition with olaparib significantly upregulated PGE_2 secretion on in *Brca1*^{mut} but not *Brca1*^{wt} cancer cells (Figure 6H). This upregulation was efficiently abrogated *in vitro* by celecoxib, a selective COX1/2 inhibitor (Figures 6H and S8G).

These data suggest that HRD ovarian cancer cells secrete lipids as a survival response to chemotherapy or PARP inhibition thereby revealing tumor-intrinsic vulnerabilities. To unleash the full immunogenicity potential of HRD TMEs, we next sought to block COX-driven prostanoid production in conjunction with dual CTX (Figure 6I and STAR Methods). We observed a statistically significant increase in the depth of tumor control in mice treated with CTX and celecoxib compared to CTX alone, which was then reflected in a prolonged disease control (Figure 6I). Mice who received CTX and celecoxib combination were then randomized (day 56) to different maintenance therapies (olaparib, olaparib + celecoxib, and olaparib + celecoxib + anti-PD-L1). Strikingly, mice receiving maintenance therapy with double combination (olaparib + celecoxib) showed a statistically significant increase in their median survival rates in comparison with mice receiving olaparib alone. This therapeutic benefit was doubled upon treatment with triple maintenance therapy (olaparib, anti-PD-L1, and celecoxib) (160 days after combinatorial treatment versus 97 days following standard CTX) (Figure 6J).

In summary, we demonstrated that intact type-I IFN signaling and by extent T cell/NK responses represent crucial drivers of anti-cancerous effects exerted by CTX during ovarian cancer treatment.

We also conclude that progression of ovarian cancers is also driven by tumor-intrinsic PGE_2 and fatty acid signaling, identifying a key vulnerability for the recurrence of human HRD OCs. Specific targeting of COX-driven PGE_2 production during chemotherapy and PARP maintenance therapy significantly prolonged relapse and survival in preclinical mouse models thus

paving the way for further exploration of differential maintenance strategies for patients with HRD OCs.

DISCUSSION

ICIs have revolutionized the immuno-oncology field but have failed to demonstrate efficacy in OC despite the ample evidence of adaptive immunity being activated at baseline. The discrepancy could rely on the poor understanding of the mechanisms that regulate the temporal evolution of the malignant and myeloid cell networks with disease progression. Immune networks vary significantly between primary and metastatic OC sites, influenced by both tumor genetics and anatomical location.[37] For example, HRD tumors of primary ovarian and fallopian tube sites harbor immune cell niches with high TIL and activated myeloid states, while distant metastatic sites show reduced immune activation.[37] Recent breakthroughs employing advanced systems' technologies (spatial proteomics and single-cell transcriptomics), start to shed light on how chemotherapy can further remodel the TME.[75,76]

Here, we applied digital pathology mIF analysis and built a tumor immune phenotype predicting algorithm which systematically classified 697 OC specimens from 5 independent multi-institutional cohorts providing the largest OC $CD8^+$-based in-tissue immune-profiling so far. Importantly, we demonstrated that patients with purely inflamed OC showed better OS and carried the highest levels of $CD8^+PD1^+$ and antigen-experienced/exhausted TILs. In addition, these tissues were characterized by increased interferon gamma and alpha activation and accompanied by activated myeloid signatures reflected in immune-stimulatory macrophages. Spatial neighborhood analysis further revealed that this small OC subset harbored intratumoral TILs:DCs niches important for response to ICIs in OC but also to adoptive T cell therapy in melanoma.[44] Altogether our results suggest that the small subgroup of purely inflamed OC identified by our algorithm could represent the ideal candidates for immunotherapy trials.

Conversely, mixed-inflamed, excluded, and desert tumors were enriched in TILs:TAMs or myeloid homotypic myeloid interactions which were associated with worse outcomes implying that TAMs could interfere with stimulatory and proficient T cell:DC interactions or exert a ''trapping effect'' of either pair population. Upon CTX pressure and recurrence, about half of OC preserved or restored their tumor immune phenotype and TILs:DCs crosstalk and those were more frequently enriched in HRD patients. Notably, tumors which amplified their TILs content at recurrence had an improved survival.

Systematically classifying the tumor immune phenotype and predicting the factors that stabilize or enrich T cells or those which exclude them from the TME at recurrence holds value for the appropriate choice of therapeutic agents upon first line treatment. Our data suggest that long-term survivors are those who carry over chromosomal instability due to loss of HRP and maintain high and homogeneous CD8 inflammation in recurrence disease. Thus, integrating genomic alterations and digital immune classification could indeed represent a combined biomarker to improve patient stratification for therapy.[31,32]

Phenocopying inflamed human OC, *Brca1*^{mut} tumors maintained activated TILs:DCs niches at recurrence and further increased the infiltration of immunostimulatory TAMs. This was enabled by immunogenic tumor cell states with increased antigen presentation and inflammatory CAFs. However, they could still evade T cell-mediated destruction likely due to the upregulation of PGE_2-producing signaling pathways known to restrict the expansion of antigen-experienced TILs and downstream destruction of IL-2 signaling and metabolic fitness impairment.[74,77,78] Our *in vivo* data further demonstrated that specific targeting of COX-driven PGE_2 production during chemotherapy and PARP maintenance therapy significantly prolonged survival in preclinical mouse models. Our data strongly encourage further exploration of the COX1/2 axis blockade in maintenance strategies for patients with BRCA1^{mut} OCs to ultimately unleash the functionality of the TILs:DCs niches and prolong disease control during CTX and PARPi.

In contrast, *Brca1*^{wt} tumors displayed concomitant loss of TILs and DCs upon CTX, alike human recurrent HRP OC. Instead, they were highly infiltrated by TAMs reprogrammed to overexpress the *Trem2/ApoE* axis involved in lipid metabolism. These was likely driven by emerging suppressive and highly metabolic malignant states with *Nduf4l2* and *Galectin3* overexpression[64,68] and characterized by signatures of the EMT-PI3K-AKT pathway, NCAM1 and LG1-ADAM interactions[79] associated with resistance to ICIs.[80] Consistently, our data showed that therapeutically targeting of TREM2 overexpressing TAMs may improve anti-tumor immune responses and delay recurrence after first-line CTX in HRP OC.

Our findings provide important mechanistic insights about the complex spatial and temporal evolution of the OC TME and provide new targets for differential treatment approaches according to BRCA/HRP status. Furthermore, they underscore that to prolong the first platinum-free interval a concerted targeted modulation of both the malignant and immune OC compartment is required.

RESOURCE AVAILABILITY

Lead contact

Further information and requests for resources should be directed to and will be fulfilled by the lead contact Dr. Denarda Dangaj Laniti (denarda.dangaj@chuv.ch).

Materials availability

This study did not generate new unique reagents.

Data and code availability

Human targeted gene panel data have been deposited at https://doi.org/10.5281/zenodo.15720518, human bulk RNA-seq data have been deposited at EGA under the following id EGAD50000001556. Mouse single-cell sequencing data will be made publicly available in the Gene Expression Omnibus (GEO) under the GSE264660 accession number at the time of publication. All code used for the data analysis are listed in the key resources table. Any additional information required to reanalyze the data reported in this paper is available from the lead contact upon request.

ACKNOWLEDGMENTS

We are grateful to the patients and their families for their dedicated collaboration.

We thank Jean-Paul Rivals and all the team from CHUV Biobank-Center of Experimental Therapeutics (CTE) for their assistance.

We thank the Lausanne Genomic Technologies Facility for bulk and single-cell DNA and RNA sequencing and Florian Huber for his assistance for bulk RNA-seq data deposition.

This work was supported by the Ludwig Institute for Cancer Research (Myeloid Cells in Cancer Initiative, MCCI project), the DOD OCA Early Career Investigator (ECI) W81XWH2210703 Award OC210038 to D.D.L, the Subaward 80863/00 to D.D.L/M.A.M (funded from the DOD W81XWH-20-1-0881 grant to OCA Deanship) and Hoffmann-La Roche AG grant (SG45079 LAU-4) to D.D.L.

For the NHS/NHSII, the authors would like to acknowledge the Channing Division of Network Medicine, Department of Medicine, Brigham and Women's Hospital, as the home of the Nurses' Health Study. The authors would also like to acknowledge the contribution to this study from central cancer registries supported through the Centers for Disease Control and Prevention's National Program of Cancer Registries (NPCR) and/or the National Cancer Institute's Surveillance, Epidemiology, and End Results (SEER) Program. Central registries may also be supported by state agencies, universities, and cancer centers.

This Research Project was partially supported by the European Society of Medical Oncology (ESMO) Translational Fellowship to E.G.

J.A.M.-J. received the support of a fellowship from 'la Caixa' Foundation (ID 100010434) which code is "LCF/BQ/DR21/11880015" and a travel fellowship from the EACR.

The research was supported by the National Institute for Health Research (NIHR) Biomedical Research Centre based at Imperial College Healthcare NHS Trust and Imperial College London. We thank Nona Rama and Naina Patel from the Experimental Cancer Medicine Center (Hammersmith Campus, Imperial College) and Kay Dawson from ICHTB for tissue collection support. P.C. and C.F. acknowledge funding from the Ovarian Fund, Imperial Health Charity.

The work in the NHS/NHSII was supported by grants from the National Institutes of Health, National Cancer Institute: UM1 CA186107; P01 CA87969; U01 CA176726; and R01CA258679 to K.L.T.

M.A.M. is supported by a DOD Ovarian Cancer Research Program, OCA Early Career Investigator Award (OC200236, W81XWH-21-1-0914). Opinions, interpretations, conclusions, and recommendations are those of the authors and are not necessarily endorsed by the DOD.

Data from this this study were shared by the EORTC Gynecological Cancer Group through the EORTC data sharing policy.

Any views, opinions, findings, conclusions, or recommendations expressed in this material are those solely of the authors.

AUTHOR CONTRIBUTIONS

E.G. and D.D.L. conceptualized the study. E.G., A.J.G., N.F., M.D., F.D.C., B.S.C., and H.J.F. performed the experiments. F.B., A.M., N.R., C.C., D.B., J.D., and M.A.M. performed the bioinformatic analysis. E.G., F.B., A.M., and A.J.G, analyzed and interpreted the data. J.D. provided pathology evaluation of the samples. P.C., E.M.S., S.A.M., J.L.T., G.C., and C.F. collected clinical samples. G.S., K.F., S.R., and S.T. provided assistance for mIF imaging analysis. A.J.M., M.M., J.A.M.J., M.J.P., L.A.K., G.C., and J.R.C.-G. provided scientific input. E.G. and D.D.L. wrote the manuscript. All authors read and approved the final version of the manuscript.

DECLARATION OF INTERESTS

E.G. received honoraria from AbbVie and Astrazeneca. C.F. received honoraria from Ethicon, GSK, Astra Zeneca/MSD, Tesaro, Clovis, Sequana and Roche, outside of the submitted work. M.M. is a current employee of the CDR-Life company. SB received research funding to the institution from Astrazeneca and GlaxoSmithKline; personal honoraria fees for advisory boards and/or educational activities from Abbvie, Astrazeneca, Biontech, Eisai, Gilead, GlaxoSmithKline, Gray Wolf Therapeutics, Immunogen, Incyte, ITM Oncologics, Merck Sharpe Dohme, Myriad, Pharmaand, Takeda, TORL BioTherapeutics, Verastem and Zymeworks; Travel expenses from Astrazeneca, GlaxoSmithKline and Verastem. In the last three years G.C. has received grants, research support or has been coinvestigator in clinical trials by Bristol-Myers Squibb, Tigen Pharma, Iovance, F. Hoffmann-La Roche AG, Boehringer Ingelheim. The Lausanne University Hospital (CHUV) has received honoraria for advisory services G.C. has provided to Genentech, AstraZeneca AG, EVIR. Patents related to the NeoTIL technology from the Coukos laboratory have been licensed by the Ludwig Institute, on behalf also of the University of Lausanne and the CHUV, to Tigen Pharma. G.C. has previously received royalties from the University of Pennsylvania for CAR-T cell therapy licensed to Novartis and Immunity Therapeutics. J.R.C.-G. has stock options with Anixa Biosciences and Alloy Therapeutics; receives licensing fees from Anixa Biosciences and consulting fees from Alloy Therapeutics; and is co-founder of Cellepus Therapeutics. D.D.L has received research grant from Hoffmann-La Roche AG and 10xGenomics. All other authors declared no competing interests.

STAR★METHODS

Detailed methods are provided in the online version of this paper and include the following:

- KEY RESOURCES TABLE
- EXPERIMENTAL MODEL AND STUDY PARTICIPANT DETAILS
  - Ethics approval
  - Human samples
  - Cell lines
  - Animal model
- METHOD DETAILS
  - FFPE slides preparation and mIF staining
  - mIF data analysis
  - Neighborhood mutual cell interaction analysis
  - Mathematical representation of mutual interaction in sets A and B
  - Tissue partitioning for mutual interaction computation
  - Cellular triplets spatial interactions
  - Survival curves
  - Targeted DNA analysis
  - Sequencing and analysis
  - Bulk RNA sequencing library preparation and processing
  - Gene expression analyses
  - Gene signatures
  - Mouse treatment
  - Whole body Bioluminescence imaging
  - Tumour processing and flow cytometry
  - Single-cell RNA sequencing
  - Cell multiplexing
  - FACS sorting
  - Encapsulation and library construction
  - Sequencing
  - Alignment, annotation and downstream analysis
  - Gene metaprogram analysis of malignant cells
  - MultiNicheNet analysis
  - Multiplex chromogenic immunohistochemistry
  - ELISA
- QUANTIFICATION AND STATISTICAL ANALYSIS

SUPPLEMENTAL INFORMATION

Supplemental information can be found online at https://doi.org/10.1016/j.ccell.2025.07.005.

Received: May 7, 2024
Revised: February 14, 2025
Accepted: July 3, 2025
Published: July 31, 2025

REFERENCES

1. Torre, L.A., Trabert, B., DeSantis, C.E., Miller, K.D., Samimi, G., Runowicz, C.D., Gaudet, M.M., Jemal, A., and Siegel, R.L. (2018). Ovarian cancer statistics, 2018. CA Cancer J. Clin. *68*, 284–296. https://doi.org/10.3322/caac.21456.

2. Ledermann, J.A., Raja, F.A., Fotopoulou, C., Gonzalez-Martin, A., Colombo, N., and Sessa, C.; ESMO Guidelines Working Group (2018). Newly diagnosed and relapsed epithelial ovarian carcinoma: ESMO Clinical Practice Guidelines for diagnosis, treatment and follow-up. Ann. Oncol. *29*, iv259. https://doi.org/10.1093/annonc/mdy157.

3. Zhang, L., Conejo-Garcia, J.R., Katsaros, D., Gimotty, P.A., Massobrio, M., Regnani, G., Makrigiannakis, A., Gray, H., Schlienger, K., Liebman, M.N., et al. (2003). Intratumoral T cells, recurrence, and survival in epithelial ovarian cancer. N. Engl. J. Med. *348*, 203–213. https://doi.org/10.1056/NEJMoa020177.

4. Ovarian Tumor Tissue Analysis (OTTA) Consortium, Goode, E.L., Block, M. S., Kalli, K.R., Vierkant, R.A., Chen, W., Fogarty, Z.C., Gentry-Maharaj, A., Tołoczko, A., Hein, A., et al. (2017). Dose-Response Association of CD8+ Tumor-Infiltrating Lymphocytes and Survival Time in High-Grade Serous Ovarian Cancer. JAMA Oncol. *3*, e173290. https://doi.org/10.1001/jamaoncol.2017.3290.

5. Sato, E., Olson, S.H., Ahn, J., Bundy, B., Nishikawa, H., Qian, F., Jungbluth, A.A., Frosina, D., Gnjatic, S., Ambrosone, C., et al. (2005). Intraepithelial CD8+ tumor-infiltrating lymphocytes and a high CD8+/regulatory T cell ratio are associated with favorable prognosis in ovarian cancer. Proc. Natl. Acad. Sci. USA *102*, 18538–18543. https://doi.org/10.1073/pnas.0509182102.

6. Launonen, I.M., Lyytikäinen, N., Casado, J., Anttila, E.A., Szabó, A., Haltia, U.M., Jacobson, C.A., Lin, J.R., Maliga, Z., Howitt, B.E., et al. (2022). Single-cell tumor-immune microenvironment of BRCA1/2 mutated high-grade serous ovarian cancer. Nat. Commun. *13*, 835. https://doi.org/10.1038/s41467-022-28389-3.

7. Matsushita, H., Hasegawa, K., Oda, K., Yamamoto, S., Asada, K., Karasaki, T., Yabuno, A., Nishijima, A., Nejo, T., Kobayashi, Y., et al. (2020). Neoantigen load and HLA-class I expression identify a subgroup of tumors with a T-cell-inflamed phenotype and favorable prognosis in homologous recombination-proficient high-grade serous ovarian carcinoma. J. Immunother. Cancer *8*, e000375. https://doi.org/10.1136/jitc-2019-000375.

8. Bronger, H. (2021). Immunology and Immune Checkpoint Inhibition in Ovarian Cancer - Current Aspects. Geburtshilfe Frauenheilkd. *81*, 1128–1144. https://doi.org/10.1055/a-1475-4335.

9. Ghisoni, E., Imbimbo, M., Zimmermann, S., and Valabrega, G. (2019). Ovarian Cancer Immunotherapy: Turning up the Heat. Int. J. Mol. Sci. *20*, 2927. https://doi.org/10.3390/ijms20122927.

10. Fridman, W.H., Zitvogel, L., Sautès–Fridman, C., and Kroemer, G. (2017). The immune contexture in cancer prognosis and treatment. Nat. Rev. Clin. Oncol. *14*, 717–734. https://doi.org/10.1038/nrclinonc.2017.101.

11. Anadon, C.M., Yu, X., Hänggi, K., Biswas, S., Chaurio, R.A., Martin, A., Payne, K.K., Mandal, G., Innamarato, P., Harro, C.M., et al. (2022). Ovarian cancer immunogenicity is governed by a narrow subset of progenitor tissue-resident memory T cells. Cancer Cell *40*, 545–557.e13. https://doi.org/10.1016/j.ccell.2022.03.008.

12. Jimenez-Sanchez, A., Memon, D., Pourpe, S., Veeraraghavan, H., Li, Y., Vargas, H.A., Gill, M.B., Park, K.J., Zivanovic, O., Konner, J., et al. (2017). Heterogeneous Tumor-Immune Microenvironments among Differentially Growing Metastases in an Ovarian Cancer Patient. Cell *170*, 927–938.e20. https://doi.org/10.1016/j.cell.2017.07.025.

13. Garsed, D.W., Pandey, A., Fereday, S., Kennedy, C.J., Takahashi, K., Alsop, K., Hamilton, P.T., Hendley, J., Chiew, Y.E., Traficante, N., et al. (2022). The genomic and immune landscape of long-term survivors of high-grade serous ovarian cancer. Nat. Genet. *54*, 1853–1864. https://doi.org/10.1038/s41588-022-01230-9.

14. Curiel, T.J., Coukos, G., Zou, L., Alvarez, X., Cheng, P., Mottram, P., Evdemon-Hogan, M., Conejo-Garcia, J.R., Zhang, L., Burow, M., et al. (2004). Specific recruitment of regulatory T cells in ovarian carcinoma fosters immune privilege and predicts reduced survival. Nat. Med. *10*, 942–949. https://doi.org/10.1038/nm1093.

15. Hornburg, M., Desbois, M., Lu, S., Guan, Y., Lo, A.A., Kaufman, S., Elrod, A., Lotstein, A., DesRochers, T.M., Munoz-Rodriguez, J.L., et al. (2021). Single-cell dissection of cellular components and interactions shaping the tumor immune phenotypes in ovarian cancer. Cancer Cell *39*, 928–944.e6. https://doi.org/10.1016/j.ccell.2021.04.004.

16. Duraiswamy, J., Turrini, R., Minasyan, A., Barras, D., Crespo, I., Grimm, A. J., Casado, J., Genolet, R., Benedetti, F., Wicky, A., et al. (2021). Myeloid antigen-presenting cell niches sustain antitumor T cells and license PD-1 blockade via CD28 costimulation. Cancer Cell *39*, 1623–1642.e20. https://doi.org/10.1016/j.ccell.2021.10.008.

17. Banville, A.C., and Nelson, B.H. (2022). Breaching B cell tolerance in the tumor microenvironment. Cancer Cell *40*, 356–358. https://doi.org/10.1016/j.ccell.2022.03.011.

18. Biswas, S., Mandal, G., Payne, K.K., Anadon, C.M., Gatenbee, C.D., Chaurio, R.A., Costich, T.L., Moran, C., Harro, C.M., Rigolizzo, K.E., et al. (2021). IgA transcytosis and antigen recognition govern ovarian cancer immunity. Nature *591*, 464–470. https://doi.org/10.1038/s41586-020-03144-0.

19. Jimenez-Sanchez, A., Cybulska, P., Mager, K.L., Koplev, S., Cast, O., Couturier, D.L., Memon, D., Selenica, P., Nikolovski, I., Mazaheri, Y., et al. (2020). Unraveling tumor-immune heterogeneity in advanced ovarian cancer uncovers immunogenic effect of chemotherapy. Nat. Genet. *52*, 582–593. https://doi.org/10.1038/s41588-020-0630-5.

20. Kandalaft, L.E., Dangaj Laniti, D., and Coukos, G. (2022). Immunobiology of high-grade serous ovarian cancer: lessons for clinical translation. Nat. Rev. Cancer *22*, 640–656. https://doi.org/10.1038/s41568-022-00503-z.

21. Zhang, A.W., McPherson, A., Milne, K., Kroeger, D.R., Hamilton, P.T., Miranda, A., Funnell, T., Little, N., de Souza, C.P., Laan, S., et al. (2018). Interfaces of Malignant and Immunologic Clonal Dynamics in Ovarian Cancer. Cell *173*, 1755–1769.e22. https://doi.org/10.1016/j.cell.2018.03.073.

22. Bohm, S., Montfort, A., Pearce, O.M., Topping, J., Chakravarty, P., Everitt, G.L., Clear, A., McDermott, J.R., Ennis, D., Dowe, T., et al. (2016). Neoadjuvant Chemotherapy Modulates the Immune Microenvironment in Metastases of Tubo-Ovarian High-Grade Serous Carcinoma. Clin. Cancer Res. *22*, 3025–3036. https://doi.org/10.1158/1078-0432.CCR-15-2657.

23. Pujade-Lauraine, E., Fujiwara, K., Ledermann, J.A., Oza, A.M., Kristeleit, R., Ray-Coquard, I.L., Richardson, G.E., Sessa, C., Yonemori, K., Banerjee, S., et al. (2021). Avelumab alone or in combination with chemotherapy versus chemotherapy alone in platinum-resistant or platinum-refractory ovarian cancer (JAVELIN Ovarian 200): an open-label, three-arm, randomised, phase 3 study. Lancet Oncol. *22*, 1034–1046. https://doi.org/10.1016/S1470-2045(21)00216-3.

24. Kurtz, J.E., Pujade-Lauraine, E., Oaknin, A., Belin, L., Leitner, K., Cibula, D., Denys, H., Rosengarten, O., Rodrigues, M., de Gregorio, N., et al. (2023). Atezolizumab Combined With Bevacizumab and Platinum-Based Therapy for Platinum-Sensitive Ovarian Cancer: Placebo-Controlled Randomized Phase III ATALANTE/ENGOT-ov29 Trial. J. Clin. Oncol. *41*, 4768–4778. https://doi.org/10.1200/JCO.23.00529.

25. Monk, B.J., Colombo, N., Oza, A.M., Fujiwara, K., Birrer, M.J., Randall, L., Poddubskaya, E.V., Scambia, G., Shparyk, Y.V., Lim, M.C., et al. (2021). Chemotherapy with or without avelumab followed by avelumab maintenance versus chemotherapy alone in patients with previously untreated epithelial ovarian cancer (JAVELIN Ovarian 100): an open-label, randomised, phase 3 trial. Lancet Oncol. *22*, 1275–1289. https://doi.org/10.1016/S1470-2045(21)00342-9.

26. Colditz, G.A., and Hankinson, S.E. (2005). The Nurses' Health Study: lifestyle and health among women. Nat. Rev. Cancer *5*, 388–396. https://doi.org/10.1038/nrc1608.

27. Hathaway, C.A., Conejo-Garcia, J.R., Fridley, B.L., Rosner, B., Saeed-Vafa, D., Moran Segura, C., Nguyen, J.V., Hecht, J.L., Sasamoto, N., Terry, K.L., et al. (2023). Measurement of Ovarian Tumor Immune Profiles by Multiplex Immunohistochemistry: Implications for Epidemiologic Studies. Cancer Epidemiol. Biomarkers Prev. *32*, 848–853. https://doi.org/10.1158/1055-9965.EPI-22-1285.

28. Gulhan, D.C., Lee, J.J.K., Melloni, G.E.M., Cortés-Ciriano, I., and Park, P. J. (2019). Detecting the mutational signature of homologous recombination deficiency in clinical samples. Nat. Genet. *51*, 912–919. https://doi.org/10.1038/s41588-019-0390-2.

29. Alexandrov, L.B., Kim, J., Haradhvala, N.J., Huang, M.N., Tian Ng, A.W., Wu, Y., Boot, A., Covington, K.R., Gordenin, D.A., Bergstrom, E.N., et al. (2020). The repertoire of mutational signatures in human cancer. Nature *578*, 94–101. https://doi.org/10.1038/s41586-020-1943-3.

30. Liu, Y.L., Selenica, P., Zhou, Q., Iasonos, A., Callahan, M., Feit, N.Z., Boland, J., Vazquez-Garcia, I., Mandelker, D., Zehir, A., et al. (2020). BRCA Mutations, Homologous DNA Repair Deficiency, Tumor Mutational Burden, and Response to Immune Checkpoint Inhibition in Recurrent Ovarian Cancer. JCO Precis. Oncol. *4*, 665–679. https://doi.org/10.1200/PO.20.00069.

31. Ghisoni, E., Morotti, M., Sarivalasis, A., Grimm, A.J., Kandalaft, L., Laniti, D.D., and Coukos, G. (2024). Immunotherapy for ovarian cancer: towards a tailored immunophenotype-based approach. Nat. Rev. Clin. Oncol. *21*, 801–817. https://doi.org/10.1038/s41571-024-00937-4.

32. Chap, B.S., Rayroux, N., Grimm, A.J., Ghisoni, E., and Dangaj Laniti, D. (2024). Crosstalk of T cells within the ovarian cancer microenvironment. Trends Cancer *10*, 1116–1130. https://doi.org/10.1016/j.trecan.2024.09.001.

33. Azizi, E., Carr, A.J., Plitas, G., Cornish, A.E., Konopacki, C., Prabhakaran, S., Nainys, J., Wu, K., Kiseliovas, V., Setty, M., et al. (2018). Single-Cell Map of Diverse Immune Phenotypes in the Breast Tumor Microenvironment. Cell *174*, 1293–1308.e36. https://doi.org/10.1016/j.cell.2018.05.060.

34. Jerby-Arnon, L., Shah, P., Cuoco, M.S., Rodman, C., Su, M.J., Melms, J. C., Leeson, R., Kanodia, A., Mei, S., Lin, J.R., et al. (2018). A Cancer Cell Program Promotes T Cell Exclusion and Resistance to Checkpoint Blockade. Cell *175*, 984–997.e24. https://doi.org/10.1016/j.cell.2018.09.006.

35. van der Leun, A.M., Thommen, D.S., and Schumacher, T.N. (2020). CD8(+) T cell states in human cancer: insights from single-cell analysis. Nat. Rev. Cancer *20*, 218–232. https://doi.org/10.1038/s41568-019-0235-4.

36. Bruand, M., Barras, D., Mina, M., Ghisoni, E., Morotti, M., Lanitis, E., Fahr, N., Desbuisson, M., Grimm, A., Zhang, H., et al. (2021). Cell-autonomous inflammation of BRCA1-deficient ovarian cancers drives both tumor-intrinsic immunoreactivity and immune resistance via STING. Cell Rep. *36*, 109412. https://doi.org/10.1016/j.celrep.2021.109412.

37. Vazquez-Garcia, I., Uhlitz, F., Ceglia, N., Lim, J.L.P., Wu, M., Mohibullah, N., Niyazov, J., Ruiz, A.E.B., Boehm, K.M., Bojilova, V., et al. (2022). Ovarian cancer mutational processes drive site-specific immune evasion. Nature *612*, 778–786. https://doi.org/10.1038/s41586-022-05496-1.

38. Zilionis, R., Engblom, C., Pfirschke, C., Savova, V., Zemmour, D., Saatcioglu, H.D., Krishnan, I., Maroni, G., Meyerovitz, C.V., Kerwin, C. M., et al. (2019). Single-Cell Transcriptomics of Human and Mouse Lung Cancers Reveals Conserved Myeloid Populations across Individuals and Species. Immunity *50*, 1317–1334.e10. https://doi.org/10.1016/j.immuni.2019.03.009.

39. Yang, Q., Zhang, H., Wei, T., Lin, A., Sun, Y., Luo, P., and Zhang, J. (2021). Single-Cell RNA Sequencing Reveals the Heterogeneity of Tumor-Associated Macrophage in Non-Small Cell Lung Cancer and Differences Between Sexes. Front. Immunol. *12*, 756722. https://doi.org/10.3389/fimmu.2021.756722.

40. Dangaj, D., Bruand, M., Grimm, A.J., Ronet, C., Barras, D., Duttagupta, P. A., Lanitis, E., Duraiswamy, J., Tanyi, J.L., Benencia, F., et al. (2019). Cooperation between Constitutive and Inducible Chemokines Enables T Cell Engraftment and Immune Attack in Solid Tumors. Cancer Cell *35*, 885–900.e10. https://doi.org/10.1016/j.ccell.2019.05.004.

41. Desbois, M., Udyavar, A.R., Ryner, L., Kozlowski, C., Guan, Y., Dürrbaum, M., Lu, S., Fortin, J.P., Koeppen, H., Ziai, J., et al. (2020). Integrated digital pathology and transcriptome analysis identifies molecular mediators of T-cell exclusion in ovarian cancer. Nat. Commun. *11*, 5583. https://doi.org/10.1038/s41467-020-19408-2.

42. Tothill, R.W., Tinker, A.V., George, J., Brown, R., Fox, S.B., Lade, S., Johnson, D.S., Trivett, M.K., Etemadmoghadam, D., Locandro, B., et al. (2008). Novel molecular subtypes of serous and endometrioid ovarian cancer linked to clinical outcome. Clin. Cancer Res. *14*, 5198–5208. https://doi.org/10.1158/1078-0432.CCR-08-0196.

43. Zhang, Y., Chen, H., Mo, H., Hu, X., Gao, R., Zhao, Y., Liu, B., Niu, L., Sun, X., Yu, X., et al. (2021). Single-cell analyses reveal key immune cell subsets associated with response to PD-L1 blockade in triple-negative breast cancer. Cancer Cell *39*, 1578–1593.e8. https://doi.org/10.1016/j.ccell.2021.09.010.

44. Barras, D., Ghisoni, E., Chiffelle, J., Orcurto, A., Dagher, J., Fahr, N., Benedetti, F., Crespo, I., Grimm, A.J., Morotti, M., et al. (2024). Response to tumor-infiltrating lymphocyte adoptive therapy is associated with preexisting CD8(+) T-myeloid cell networks in melanoma. Sci. Immunol. *9*, eadg7995. https://doi.org/10.1126/sciimmunol.adg7995.

45. Li, H., van der Leun, A.M., Yofe, I., Lubling, Y., Gelbard-Solodkin, D., van Akkooi, A.C., van den Braber, M., Rozeman, E.A., Haanen, J.B., Blank, C. U., et al. (2019). Dysfunctional CD8 T Cells Form a Proliferative, Dynamically Regulated Compartment within Human Melanoma. Cell *176*, 775–789.e18. https://doi.org/10.1016/j.cell.2018.11.043.

46. Pittet, M.J., Di Pilato, M., Garris, C., and Mempel, T.R. (2023). Dendritic cells as shepherds of T cell immunity in cancer. Immunity *56*, 2218–2230. https://doi.org/10.1016/j.immuni.2023.08.014.

47. Garris, C.S., Arlauckas, S.P., Kohler, R.H., Trefny, M.P., Garren, S., Piot, C., Engblom, C., Pfirschke, C., Siwicki, M., Gungabeesoon, J., et al. (2018). Successful Anti-PD-1 Cancer Immunotherapy Requires T Cell-Dendritic Cell Crosstalk Involving the Cytokines IFN-gamma and IL-12. Immunity *49*, 1148–1161.e7. https://doi.org/10.1016/j.immuni.2018.09.024.

48. Kersten, K., Hu, K.H., Combes, A.J., Samad, B., Harwin, T., Ray, A., Rao, A.A., Cai, E., Marchuk, K., Artichoker, J., et al. (2022). Spatiotemporal co-dependency between macrophages and exhausted CD8(+) T cells in cancer. Cancer Cell *40*, 624–638.e9. https://doi.org/10.1016/j.ccell.2022.05.004.

49. Banerjee, S., Ghisoni, E., Wolfer, A., Ottevanger, P.B., Le Scodan, R., Sarivalasis, A., Montes, A., Kroep, J., Romeo Marin, M., Szturz, P., et al. (2025). Bevacizumab, Atezolizumab, and Acetylsalicylic Acid in Recurrent, Platinum-Resistant Ovarian Cancer: The EORTC 1508-GCG Phase II Study. Clin. Cancer Res. *31*, 2145–2153. https://doi.org/10.1158/1078-0432.CCR-24-3368.

50. Burdett, N.L., Willis, M.O., Alsop, K., Hunt, A.L., Pandey, A., Hamilton, P. T., Abulez, T., Liu, X., Hoang, T., Craig, S., et al. (2023). Multiomic analysis of homologous recombination-deficient end-stage high-grade serous ovarian cancer. Nat. Genet. *55*, 437–450. https://doi.org/10.1038/s41588-023-01320-2.

51. Walton, J., Blagih, J., Ennis, D., Leung, E., Dowson, S., Farquharson, M., Tookman, L.A., Orange, C., Athineos, D., Mason, S., et al. (2016). CRISPR/Cas9-Mediated Trp53 and Brca2 Knockout to Generate Improved Murine Models of Ovarian High-Grade Serous Carcinoma. Cancer Res. *76*, 6118–6129. https://doi.org/10.1158/0008-5472.CAN-16-1272.

52. Walton, J.B., Farquharson, M., Mason, S., Port, J., Kruspig, B., Dowson, S., Stevenson, D., Murphy, D., Matzuk, M., Kim, J., et al. (2017). CRISPR/Cas9-derived models of ovarian high grade serous carcinoma targeting Brca1, Pten and Nf1, and correlation with platinum sensitivity. Sci. Rep. *7*, 16827. https://doi.org/10.1038/s41598-017-17119-1.

53. Scarlett, U.K., Rutkowski, M.R., Rauwerdink, A.M., Fields, J., Escovar-Fadul, X., Baird, J., Cubillos-Ruiz, J.R., Jacobs, A.C., Gonzalez, J.L., Weaver, J., et al. (2012). Ovarian cancer progression is controlled by phenotypic changes in dendritic cells. J. Exp. Med. *209*, 495–506. https://doi.org/10.1084/jem.20111413.

54. Grout, J.A., Sirven, P., Leader, A.M., Maskey, S., Hector, E., Puisieux, I., Steffan, F., Cheng, E., Tung, N., Maurin, M., et al. (2022). Spatial Positioning and Matrix Programs of Cancer-Associated Fibroblasts Promote T-cell Exclusion in Human Lung Tumors. Cancer Discov. *12*, 2606–2625. https://doi.org/10.1158/2159-8290.CD-21-1714.

55. Hanley, C.J., Waise, S., Ellis, M.J., Lopez, M.A., Pun, W.Y., Taylor, J., Parker, R., Kimbley, L.M., Chee, S.J., Shaw, E.C., et al. (2023). Single-cell analysis reveals prognostic fibroblast subpopulations linked to molecular and immunological subtypes of lung cancer. Nat. Commun. *14*, 387. https://doi.org/10.1038/s41467-023-35832-6.

56. Colonna, M. (2023). The biology of TREM receptors. Nat. Rev. Immunol. *23*, 580–594. https://doi.org/10.1038/s41577-023-00837-1.

57. Binnewies, M., Pollack, J.L., Rudolph, J., Dash, S., Abushawish, M., Lee, T., Jahchan, N.S., Canaday, P., Lu, E., Norng, M., et al. (2021). Targeting TREM2 on tumor-associated macrophages enhances immunotherapy. Cell Rep. *37*, 109844. https://doi.org/10.1016/j.celrep.2021.109844.

58. Capece, D., Verzella, D., Flati, I., Arboretto, P., Cornice, J., and Franzoso, G. (2022). NF-kappaB: blending metabolism, immunity, and inflammation. Trends Immunol. *43*, 757–775. https://doi.org/10.1016/j.it.2022.07.004.

59. Hoover, A.A., Hufnagel, D.H., Harris, W., Bullock, K., Glass, E.B., Liu, E., Barham, W., Crispens, M.A., Khabele, D., Giorgio, T.D., et al. (2020). Increased canonical NF-kappaB signaling specifically in macrophages is sufficient to limit tumor progression in syngeneic murine models of ovarian cancer. BMC Cancer *20*, 970. https://doi.org/10.1186/s12885-020-07450-8.

60. Browaeys, R., Gilis, J., Sang-Aram, C., De Bleser, P., Hoste, L., Tavernier, S., Lambrechts, D., Seurinck, R., and Saeys, Y. (2023). MultiNicheNet: A Flexible Framework for Differential Cell-Cell Communication Analysis from Multi-Sample Multi-Condition Single-Cell Transcriptomics Data. https://doi.org/10.1101/2023.06.13.544751.

61. Kumari, A., Shonibare, Z., Monavarian, M., Arend, R.C., Lee, N.Y., Inman, G.J., and Mythreye, K. (2021). TGFbeta signaling networks in ovarian cancer progression and plasticity. Clin. Exp. Metastasis *38*, 139–161. https://doi.org/10.1007/s10585-021-10077-z.

62. Pietila, E.A., Gonzalez-Molina, J., Moyano-Galceran, L., Jamalzadeh, S., Zhang, K., Lehtinen, L., Turunen, S.P., Martins, T.A., Gultekin, O., Lamminen, T., et al. (2021). Co-evolution of matrisome and adaptive adhesion dynamics drives ovarian cancer chemoresistance. Nat. Commun. *12*, 3904. https://doi.org/10.1038/s41467-021-24009-8.

63. Hao, X., Zhao, B., Zhou, W., Liu, H., Fukumoto, T., Gabrilovich, D., and Zhang, R. (2021). Sensitization of ovarian tumor to immune checkpoint blockade by boosting senescence-associated secretory phenotype. iScience *24*, 102016. https://doi.org/10.1016/j.isci.2020.102016.

64. Chen, Z., Wei, X., Wang, X., Zheng, X., Chang, B., Shen, L., Zhu, H., Yang, M., Li, S., and Zheng, X. (2021). NDUFA4L2 promotes glioblastoma progression, is associated with poor survival, and can be effectively targeted by apatinib. Cell Death Dis. *12*, 377. https://doi.org/10.1038/s41419-021-03646-3.

65. Yerly, L., Andreatta, M., Garnica, J., Nardin, C., Domizio, J.D., Aubin, F., Gilliet, M., Carmona, S.J., and Kuonen, F. (2024). Wounding triggers invasive progression in human basal cell carcinoma. Preprint at bioRxiv. https://doi.org/10.1101/2024.05.31.596823.

66. Palakurthi, S., Kuraguchi, M., Zacharek, S.J., Zudaire, E., Huang, W., Bonal, D.M., Liu, J., Dhaneshwar, A., DePeaux, K., Gowaski, M.R., et al. (2019). The Combined Effect of FGFR Inhibition and PD-1 Blockade Promotes Tumor-Intrinsic Induction of Antitumor Immunity. Cancer Immunol. Res. *7*, 1457–1471. https://doi.org/10.1158/2326-6066.CIR-18-0595.

67. Mandula, J.K., Chang, S., Mohamed, E., Jimenez, R., Sierra-Mondragon, R.A., Chang, D.C., Obermayer, A.N., Moran-Segura, C.M., Das, S., Vazquez-Martinez, J.A., et al. (2022). Ablation of the endoplasmic reticulum stress kinase PERK induces paraptosis and type I interferon to promote anti-tumor T cell responses. Cancer Cell *40*, 1145–1160.e9. https://doi.org/10.1016/j.ccell.2022.08.016.

68. Zhang, P., Zhang, P., Shi, B., Zhou, M., Jiang, H., Zhang, H., Pan, X., Gao, H., Sun, H., and Li, Z. (2014). Galectin-1 overexpression promotes progression and chemoresistance to cisplatin in epithelial ovarian cancer. Cell Death Dis. *5*, e991. https://doi.org/10.1038/cddis.2013.526.

69. Liu, F.T., and Stowell, S.R. (2023). The role of galectins in immunity and infection. Nat. Rev. Immunol. *23*, 479–494. https://doi.org/10.1038/s41577-022-00829-7.

70. Tirosh, I., Izar, B., Prakadan, S.M., Wadsworth, M.H., II, Treacy, D., Trombetta, J.J., Rotem, A., Rodman, C., Lian, C., Murphy, G., et al. (2016). Dissecting the multicellular ecosystem of metastatic melanoma by single-cell RNA-seq. Science *352*, 189–196. https://doi.org/10.1126/science.aad0501.

71. Yan, T., Qiu, W., Weng, H., Fan, Y., Zhou, G., and Yang, Z. (2021). Single-Cell Transcriptomic Analysis of Ecosystems in Papillary Thyroid Carcinoma Progression. Front. Endocrinol. *12*, 729565. https://doi.org/10.3389/fendo.2021.729565.

72. Smith, P., Bradley, T., Gavarró, L.M., Goranova, T., Ennis, D.P., Mirza, H.B., De Silva, D., Piskorz, A.M., Sauer, C.M., Al-Khalidi, S., et al. (2023). The copy number and mutational landscape of recurrent ovarian high-grade serous carcinoma. Nat. Commun. *14*, 4387. https://doi.org/10.1038/s41467-023-39867-7.

73. Sandoval, T.A., Salvagno, C., Chae, C.S., Awasthi, D., Giovanelli, P., Marin Falco, M., Hwang, S.M., Teran-Cabanillas, E., Suominen, L., Yamazaki, T., et al. (2024). Iron Chelation Therapy Elicits Innate Immune Control of Metastatic Ovarian Cancer. Cancer Discov. *14*, 1901–1921. https://doi.org/10.1158/2159-8290.CD-23-1451.

74. Morotti, M., Grimm, A.J., Hope, H.C., Arnaud, M., Desbuisson, M., Rayroux, N., Barras, D., Masid, M., Murgues, B., Chap, B.S., et al. (2024). PGE(2) inhibits TIL expansion by disrupting IL-2 signalling and mitochondrial function. Nature *629*, 426–434. https://doi.org/10.1038/s41586-024-07352-w.

75. Launonen, I.M., Niemiec, I., Hincapié-Otero, M., Erkan, E.P., Junquera, A., Afenteva, D., Falco, M.M., Liang, Z., Salko, M., Chamchougia, F., et al. (2024). Chemotherapy induces myeloid-driven spatially confined T cell exhaustion in ovarian cancer. Cancer Cell *42*, 2045–2063.e10. https://doi.org/10.1016/j.ccell.2024.11.005.

76. Elorbany, S., Berlato, C., Carnevalli, L.S., Maniati, E., Barry, S.T., Wang, J., Manchanda, R., Kzhyshkowska, J., and Balkwill, F. (2024). Immunotherapy that improves response to chemotherapy in high-grade serous ovarian cancer. Nat. Commun. *15*, 10144. https://doi.org/10.1038/s41467-024-54295-x.

77. Lacher, S.B., Dörr, J., de Almeida, G.P., Hönninger, J., Bayerl, F., Hirschberger, A., Pedde, A.M., Meiser, P., Ramsauer, L., Rudolph, T.J., et al. (2024). PGE(2) limits effector expansion of tumour-infiltrating stem-like CD8(+) T cells. Nature *629*, 417–425. https://doi.org/10.1038/s41586-024-07254-x.

78. Elewaut, A., Estivill, G., Bayerl, F., Castillon, L., Novatchkova, M., Pottendorfer, E., Hoffmann-Haas, L., Schönlein, M., Nguyen, T.V., Lauss, M., et al. (2025). Cancer cells impair monocyte-mediated T cell stimulation to evade immunity. Nature *637*, 716–725. https://doi.org/10.1038/s41586-024-08257-4.

79. Zecchini, S., Bombardelli, L., Decio, A., Bianchi, M., Mazzarol, G., Sanguineti, F., Aletti, G., Maddaluno, L., Berezin, V., Bock, E., et al. (2011). The adhesion molecule NCAM promotes ovarian cancer progression via FGFR signalling. EMBO Mol. Med. *3*, 480–494. https://doi.org/10.1002/emmm.201100152.

80. Ni, Y., Soliman, A., Joehlin-Price, A., Rose, P.G., Vlad, A., Edwards, R.P., and Mahdi, H. (2021). High TGF-beta signature predicts immunotherapy resistance in gynecologic cancer patients treated with immune checkpoint inhibition. npj Precis. Oncol. *5*, 101. https://doi.org/10.1038/s41698-021-00242-8.

81. Pennington, K.P., Walsh, T., Harrell, M.I., Lee, M.K., Pennil, C.C., Rendi, M.H., Thornton, A., Norquist, B.M., Casadei, S., Nord, A.S., et al. (2014). Germline and somatic mutations in homologous recombination genes predict platinum response and survival in ovarian, fallopian tube, and peritoneal carcinomas. Clin. Cancer Res. *20*, 764–775. https://doi.org/10.1158/1078-0432.CCR-13-2287.

82. Bernards, S.S., Norquist, B.M., Harrell, M.I., Agnew, K.J., Lee, M.K., Walsh, T., and Swisher, E.M. (2016). Genetic characterization of early onset ovarian carcinoma. Gynecol. Oncol. *140*, 221–225. https://doi.org/10.1016/j.ygyno.2015.12.017.

83. Norquist, B.M., Brady, M.F., Harrell, M.I., Walsh, T., Lee, M.K., Gulsuner, S., Bernards, S.S., Casadei, S., Burger, R.A., Tewari, K.S., et al. (2018). Mutations in Homologous Recombination Genes and Outcomes in Ovarian Carcinoma Patients in GOG 218: An NRG Oncology/Gynecologic Oncology Group Study. Clin. Cancer Res. *24*, 777–783. https://doi.org/10.1158/1078-0432.CCR-17-1327.

84. Stuart, T., Butler, A., Hoffman, P., Hafemeister, C., Papalexi, E., Mauck, W. M., III, Hao, Y., Stoeckius, M., Smibert, P., and Satija, R. (2019). Comprehensive Integration of Single-Cell Data. Cell *177*, 1888–1902. e21. https://doi.org/10.1016/j.cell.2019.05.031.

STAR★METHODS

KEY RESOURCES TABLE

REAGENT or RESOURCE	SOURCE	IDENTIFIER
Antibodies		
Rabbit monoclonal anti-CD8 (clone SP16)	CellMarque	Cat#108R-16
Mouse monoclonal anti-CD11c (clone 5D11)	CellMarque	Cat#111M-16
Mouse monoclonal anti-PD1 (clone NAT105)	BioCare	Cat#ACI3137C
Rabbit monoclonal anti-PD-L1 (clone E1L3N)	CellSignaling	Cat#-13684S
Mouse monoclonal anti-CD68 (clone PG-M1)	Dako Omnis	Cat#GA613
Mouse monoclonal anti-panCK (clone AE1/AE3)	Dako Omnis	Cat#M3515
Rat IgG2b anti mouse CD45 BV785 (clone 30F11)	Biolegend	Cat#103149
Mouse IgG2a anti mouse CD161 BV711 (clone PK136)	Biolegend	Cat#108745
Rat IgG2a anti mouse CD14 BUV737 (clone Sa14-2)	BD (optibuild)	Cat#756779
Rat IgG2a anti mouse F4/80 PE (clone BM8)	Biolegend	Cat#123110
Rat IgG2b anti mouse CD11b (clone M170)	Thermo Fisher Scientific	Cat#25-0112-82
Rat IgG2b anti mouse CD3 Pacific Blue (clone 17A2)	Biolegend	Cat#100214
Rat IgG2a anti mouse CD8 BV650 (clone 53-6.7)	Biolegend	Cat#100742
Rat IgG2a anti mouse PD1 BV510 (clone 29F.1A12)	Biolegend	Cat#135241
Rat IgG2a anti mouse CD39 PECy7 (clone Duha59)	Biolegend	Cat#143806
Human monoclonal anti-CD45 (clone HI30)	Biolegend	Cat#304012
Anti-PDL1 (clone 10F.9G2, mouse IgG2b)	BioXcell	Cat#BE0101
Anti-IFNAR (clone MAR1-5A3, mouse IgG1)	Assay Genie	Cat#IVMB0202
Anti-CSFR (clone AFS98, mouse IgG2a)	Assay Genie	Cat#IVMB0001
Anti-TREM2 (clone 178, mouse IgG2a)	Assay Genie	Cat# IVMB0399
Rabbit anti pan-CK	Novus Biologicals	Cat#NB600-579
Rat anti-CD8a (clone 4SM15)	Thermo Fisher	Cat#14-0808-82
Rabbit anti-CD11c (clone D1V9Y)	Cell Signaling	Cat# 97585S
Anti-human CD3 (clone SP7)	ThermoFisher	Cat#MA5-14524
Anti-human CD8 (clone C8/144B)	DAKO	Cat#M7103
Anti-human CD103(clone SP301)	Abcam	Cat#ab227697
Anti-human CD69 (clone EPR21814)	Abcam	Cat# ab233396
Anti-human pan-CK (clone M3515)	DAKO	Cat# M3515
Anti-human CD68 (clone D4B9C)	CST	Cat#76437
Anti-human pSTAT-1 (clone 9167s)	CST	Cat#9167
Zombie UV Fixable Viability Kit	Biolegend	Cat# 423107
Foxp3/Transcription Factor kit	Thermo Fisher scientific	Cat#00-5523-00
Biological samples		
Human ovarian cancer (IMCOL primary-recurrent cohort)	Imperial College of London, UK	This paper, Table S1A
Human ovarian cancer (UPENN primary-recurrent cohort)	University of Pennsylvania, USA	This paper, Table S1B
Human ovarian cancer (UPENN-HiTide primary cohort)	University of Pennsylvania, USA	This paper, Table S2A
Human ovarian cancer tissue microarray tissues (NHS I/II cohorts, treatment-naive tissues)	Channing Division of Network Medicine, Department of Medicine, Brigham and Women's Hospital and Harvard Medical School, Boston, MA, USA	

(*Continued on next page*)

Continued

REAGENT or RESOURCE	SOURCE	IDENTIFIER
Human ovarian cancer FFPE tissues (EORTC-1508 study, recurrent cohort)	The EORTC-1508 study	EudraCT 2015-004601-17 / NCT02659384
Chemicals, peptides, and recombinant proteins		
Deparaffinization solution	Qiagen	Cat#19093
FcR blocking reagent Human	Miltenyi Biotec	Cat#130-059901
RNasin Plus RNase Inhibitor	Promega	Cat#N2618
Bovine Serum Albumin	Sigma-Aldrich	Cat#A2153
DAPI	Invitrogen	Cat#D1306
DTT	Sigma-Aldrich	Cat#43816
Luciferin	Biosynth	Cat#L-8220
Carboplatin	Accord	Cat#7504554
Paclitaxel	Labatec	Cat#4670594
Olaparib	APExBIO	Cat#A4154
Celecoxib oral	Sandoz	N/A
Poly(ethylene glycol) 300	Sigma-Aldrich	Cat#202371
Critical commercial assays		
QiAmp DNA FFPE tissue kit	Qiagen	Cat#56404
Qubit dsDNA HS assay kit	Invitrogen	Cat#Q32851
Archer VariantPlex® kit for Illumina – HS BRCA custom panel	Archer	Cat#DB0170
Archer® MBC Adapters A1-A8 for Illumina®	Archer	Cat#SA0040
RNeasy Kit mini	Qiagen	Cat#74104
Qubit RNA SS assay kit	Invitrogen	Cat#Q10210
HS NGS Fragment analyzer kit	Agilent	Cat#DNF-474-0500
Chromium Next GEM Single 3' Kit v3.1,16 rxns	10X Genomics	Cat#1000268
Chromium Next GEM Chip G Single Cell Kit, 48 rxns	10X Genomics	Cat#1000120
3′ Feature Barcode Kit, 16 rxns PN-1000262	10X Genomics	Cat#1000262
3′ CellPlex Kit Set A, 48 rxns	10X Genomics	Cat#1000261
Dual Index Kit TT Set A, 96 rxns	10X Genomics	Cat#1000215
Dual Index Kit NN Set A, 96 rxns	10X Genomics	Cat#1000243
Deposited data		
Human targeted DNA panel	This paper	Zenodo https://doi.org/10.5281/zenodo.15720518
Human bulk RNA genes signatures	This paper	EGA EGAD50000001556
Mouse single-cell RNA sequencing data	This paper	GEO GSE264660
Experimental models: Cell lines		
ID8 Trp53$^{-/-}$ and ID8 Trp53$^{-/-}$Brca1$^{-/-}$	Prof. Iain A. McNeish lab	(Walton et al., 2016[51]; Walton et al., 2017[52])
Experimental models: Organisms/strains		
C57BL/6NHsd	Inotiv	044
Software and algorithms		
Immunophenotype classification algorithm	This paper	GitiHub.com/dangajlab/Ovarian-TME
GraphPad Prism v.10	GraphPad Software, Inc	RRID: SCR-002798
Inform v. 2.5.1	Akoya Bioscience	
Phenochart v. 1.0.12	Akoya Bioscience	
FlowJO	Treestar	RRID:SCR_008520
Next-Generation Clustered Heat Map Viewer	https://www.ngchm.net/Downloads/ngChmApp.html	
Integrative Genomics Viewer	https://igv.org	

EXPERIMENTAL MODEL AND STUDY PARTICIPANT DETAILS

Ethics approval

This study received central approval by the University Hospital of Lausanne UNIL-CHUV ("Tumor heterogeneity in epithelial ovarian cancer [PB_2022-00024]) and Ludwig Cancer Research Lausanne Branch institutional review board. The study protocol for the NHS/NHSII cohorts was approved by the institutional review boards of the Brigham and Women's Hospital and Harvard T.H. Chan School of Public Health, and those of participating registries as required. All procedures were performed according to the Declaration of Helsinki guidelines. All cohorts (except for NHS/NHSII) were transferred to Lausanne under Standard Material Transfer Agreements for De-identified Human Tissues and Specimens Between Non-profit Organizations.

Human samples

IMCOL primary-recurrent cohort

Forty-six patient-matched formalin-fixed paraffin-embedded (FFPE) ovarian cancer (OC) tumor samples from 23 patients were collected at the Imperial College of London at primary surgery and first recurrence (Table S1 for patients' clinical details). The cohort was pre-selected to be a fully platinum-sensitive cohort as reflected by the long first platinum-free interval calculated from the last day of dosage of the platinum-based chemotherapy to disease relapse (Figure S1D). The project was performed under the Hammersmith and Queen Charlotte's and Chelsea Research and CHUV Ethics Committee approvals (PB_2022-00024) and human samples for this research project were collated by the Imperial College Healthcare Tissue Bank (ICHTB). ICHTB is approved by Wales REC3 to release human material for research (22/WA/2836) and samples were issued under full patient consent. ICHTB is supported by the National Institute for Health Research (NIHR) Biomedical Research Centre based at Imperial College Healthcare NHS Trust and Imperial College London. Samples were used for multiplexed immunofluorescence (mIF) analysis and somatic targeted DNA sequencing as described below.

UPENN primary-recurrent cohort

A total of 124 FFPE OC tumor samples (n=74 primary and n=50 recurrent samples respectively, from 46 patients) were collected at primary surgery and first recurrence under a protocol approved by the University of Pennsylvania Institutional Review Board and provided by the Tumor Tissue and Biospecimen Bank (TTAB), Department of Pathology, at the University of Pennsylvania, Philadelphia, USA. Detailed clinical data and samples information are reported in Table S1. Sample were used for mIF analysis and somatic targeted DNA sequencing.

HiTide-UPENN primary cohort

Fifty-one FFPE samples and n=71 snap-frozen samples were collected from 51 patients at the Ovarian Cancer Center, Department of Obstetrics & Gynecology, University of Pennsylvania, Philadelphia, USA. Informed consent was obtained from all subjects included in this study under an approved protocol from the Institutional Review Board (UPCC 17909, IRB 702679) under the care of Dr. DJ Powell and Dr. J Tanyi. Samples were collected from unselected consecutive patients ("all comers") undergoing surgery for primary stage III or IV high-grade serous ovarian cancer, as well as from the fallopian tube or primary peritoneal origin. Detailed clinical data are reported in Table S2. Samples were used for mIF analysis, bulk RNAsequencing and somatic DNA sequencing by the BROCA panel (performed by Dr E. Swisher).

NHS I/II cohort

Information including the procedures to obtain and access data from the Nurses' Health Studies (NHS and NHSII) is described at https://www.nurseshealthstudy.org/researchers (contact email: nhsaccess@channing.harvard.edu) and https://sites.sph.harvard.edu/hpfs/for-collaborators/. Because of participant confidentiality and privacy concerns, data cannot be shared publicly and requests to access NHS/NHSII data must be submitted in writing. According to standard controlled access procedures, applications to use NHS/NHSII resources will be reviewed by our External Collaborations Committee to verify that the proposed use maintains the protection of the privacy of participants and the confidentiality of the data. Investigators wishing to use NHS/NHSII data are asked to submit a brief description of the proposed project (go to https://www.nurseshealthstudy.org/researchers (contact email: nhsaccess@channing.harvard.edu) and https://sites.sph.harvard.edu/hpfs/for-collaborators/ for details. Participating central cancer registries include the following: Alabama, Alaska, Arizona, Arkansas, California, Delaware, Colorado, Connecticut, Florida, Georgia, Hawaii, Idaho, Indiana, Iowa, Kentucky, Louisiana, Maine, Maryland, Massachusetts, Michigan, Mississippi, Montana, Nebraska, Nevada, New Hampshire, New Jersey, New Mexico, New York, North Carolina, North Dakota, Ohio, Oklahoma, Oregon, Pennsylvania, Puerto Rico, Rhode Island, Seattle SEER Registry, South Carolina, Tennessee, Texas, Utah, Virginia, West Virginia, Wyoming.

Cell lines

ID8 *Trp53*$^{-/-}$*Brca1*^{wt} and *Trp53*$^{-/-}$*Brca1*^{mut} mouse OC cell lines, obtained from the laboratory of Prof. Iain A. McNeish (Institute of Cancer Sciences, University of Glasgow, Scotland)[51,52] were transduced to express luciferase[36] and cultured in DMEM supplemented with 4% FBS, 100 μg/mL penicillin, 100 μg/mL streptomycin, and ITS 35 (5μg/mL insulin, 5μg/mL transferrin, and 5ng/mL sodium selenite). Cell lines were negative for Mycoplasma contamination.

Animal model

C57BL/6NHsd female mice were obtained from Inotiv and were maintained in pathogen-free conditions. Age-matched mice 7 weeks were used for all experiments. Animal experimentation procedures were performed according to the protocols approved by the Veterinary Authorities of the Canton Vaud (VD3480d, VD3480x1, VD3480x1b, VD3480x1c), according to Swiss law.

METHOD DETAILS

FFPE slides preparation and mIF staining

Slides were prepared at the Immune Landscape Laboratory (ILL) at the Center for Experimental Therapeutics (CTE) of the Department of Oncology at CHUV (Lausanne, Switzerland) from the FFPE blocks provided. The first slide was used for H&E staining and review by a dedicated Pathologist (JD) to define the quality of tumor and stromal areas and exclude adjacent healthy tissue. A second slide of 3.5 um was used for mIF. Slides to be stained were thawed and heated at 60°C for 1 hour. mIF panels were run using the multiplex Ventana Discovery ULTRA Staining module autostainer (Roche). Slides were placed on the staining module for the deparaffinization step, consisting of 3 cycles of 8 minutes at 69°C (Discovery Wash, Ventana Roche), followed by epitope retrieval for 64 minutes at 95°C or 98°C (according to the panel protocol performed) in high pH buffer Cell Conditioning 1 (CC1, Ventana Roche) and endogenous peroxidase quenching (Discovery Inhibitor, Ventana Roche). The automated immunofluorescence (IF) staining procedure consists of multiple consecutive rounds (6 for a 7-plex) of staining. Each round includes non-specific sites blocking (Ventana, Discovery Inhibitor and Discovery Goat Ig Block), incubation with unlabeled primary antibody, followed by incubation with horseradish peroxidase (HRP)-conjugated secondary antibodies (Discovery OmniMap anti-Rabbit (Rb) and anti-Mouse (Ms), Ventana), and OpalTM (Akoya) reactive fluorophore (Opal 480, 520, 570, 620, 690, 780) detection that covalently labels the primary epitope. Then an antibody (both primary and secondary) heat denaturation step was performed prior to the next round of antibody staining. Finally, Spectral DAPI (Akoya) was used for nuclear staining. The complete list of the validated antibodies is reported in the key resources table related to STAR Methods). mIF images were acquired on the Vectra® Polaris automated quantitative pathology imaging system (Akoya Biosciences). This multispectral imaging system uses the MOTiF technology, allowing the unmixing of spectrally overlapping fluorophores and tissue autofluorescence of whole slide scans. For the optimal IF signal unmixing (individual spectral peaks) and the subsequent multiplex analysis, a spectral library containing the individual emitting spectral peaks of all fluorophores was created. For this, single antibody-coupled with fluorophore staining under the optimized conditions without DAPI, and a DAPI single staining, were performed. In addition, auto-fluorescence controls were performed by staining tumor tissue slides omitting both the fluorophore and DAPI.

mIF data analysis

Cell-densities and immune-classification algorithm

Using the Phenochart™ whole-slide viewer, regions of interest (ROIs, 931um x 698 um, range 5-110 ROIs per section) representative of the entire FFPE tissue sample were acquired. InForm 2.5.1 (Akoya Biosciences) software was used for training and phenotyping analysis. The images were first segmented into specific tissue categories of tumor, stroma and no tissue, based on pancytokeratin (panCK^{+}) and DAPI staining using the Inform Tissue Finder™ algorithm. Individual cells were then segmented using the counterstained-based adaptive cell segmentation algorithm. Quantification of the immune cells was then performed using the Inform active learning phenotyping algorithm by assigning the different cell phenotypes across several images chosen for the project. IF-stained cohorts were then batch processed and data were exported via an in-house developed R-script algorithm (Post-InForm) to retrieve single-cell x,y coordinates and staining positivity. To calculate cell densities, we counted the number of a specific cell phenotype in

both tumor and stromal compartment across the whole FFPE tissue section. Counts of each specific cell type (tissue-specific) were then divided by the area of the tissue (mm^2) to obtain a density (number of cells/mm^2).

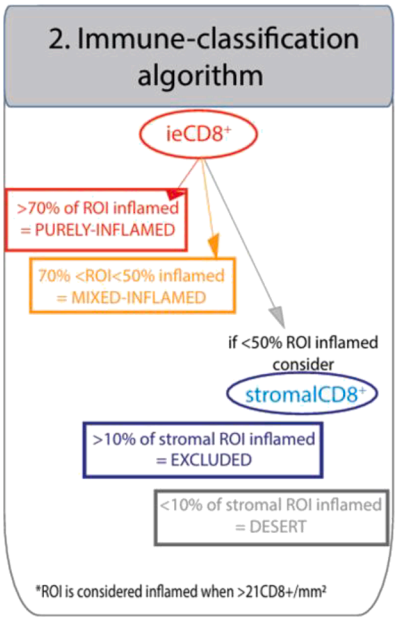

We then developed a two-step algorithm to define a $CD8^+$ T cells-based immune classifier considering not the average cell density across the whole tissue but the heterogeneous $CD8^+$ T cells distribution within tumor/stroma compartments of each ROI. First, we computed the fraction of inflamed subregions (ROIs with >21 $CD8^+$cells/mm^2) in tumor and named the sample purely inflamed if the percentage of inflamed ROIs was >70% and as mixed inflamed when this percentage was between 50% and 70%. Second, in case less than 50% of ROIs were inflamed in the tumor, we considered the sample as excluded if >10% of ROIs showed >21 $CD8^+$ cells/mm^2 in the stroma and as desert if this percentage was <10%.

To adapt our code to the NHS I/II study cohort from which only tumor micro-arrays (TMAs, average size 0.6 mm in diameter) were available, we first selected only the TMAs where $CD8^+$ staining was present. We assigned to each TMA a unique identifier (ID) corresponding to the patient from whom the core was obtained. The distribution of cores per patient ID varies from 1 to 15 cores, with a median of 6 cores per patient. For each core including CD8 marker, we then calculated the density of total $CD8^+$ cells in both the tumor and stromal compartments. To ensure consistency with the previous approach, only patients with a minimum of three different TMAs including CD8 were considered, while samples with less than three cores were excluded from further analyses. Therefore, a total of N=418 unique patients (and respective TMAs) were included in the immune classification prediction using a similar approach to that applied in the previous cohorts (IMCOL, UPENN and HiTide-UPENN), treating each core as a separate ROI.

Neighborhood mutual cell interaction analysis

Starting from previous published works[16,36] we computed a new "mutual interactions" methodology which takes into consideration "bi-directional" cells interaction from two different cell types. Normalization by the proportions of both cell types of interest on a surface (i.e. tumor or stroma regions) was applied to avoid cell abundance bias. In our specific case, the total area, can be split into tumoral regions (defined by the presence of the $panCK^+$ protein marker) and stromal regions (defined by the absence of $panCK^+$) where we can measure the neighboring of a point (i.e. cell) (defined as starting point) of type "A" (i.e. cell type A) of coordinates (xa, ya), with type "B" points (i.e. cells from cell type B; defined as ending points) in the surrounding area within a predefined distance (i.e. 20um). The distance between point "A" (i.e. cell type A) and a point "B" (i.e. cell type B), with coordinates (x, y), is then defined as the Euclidean distance D:

$$D = \sqrt{(x_a - x_b)^2 - (y_a - y_b)^2}$$

A point "A", and a point "B" are then considered neighbors, if the distance "D", between "A" and "B" is less than a given threshold (ε). Such definition can be visualized as a circular surrounding of the point A with a radius equal to the threshold (ε, that is 20um in our case).

Given two sets of points in a two-dimensional space we could implement a measure that estimate their vicinity. This measure is called mutual interaction.[44]

Given the set of points (i.e. cells) A={A1, …., AN}, and the set of points (i.e. cells) B={B1, …, BK}, for each point of the set "A" we measure if there is, at least, an element of the set "B" at a distance D< ε. For a given point, if the condition is true, such a point has at

least one neighbor of type "B". We then sum all the points of the set A that have at least one neighbor of type "B". We repeat such procedure, but now starting from the points of the set "B" looking for neighbors in the set "A".

The mutual interaction is them computed as:

(number of A with a neighbor B) + (number of B with a neighbor A) / (Number of A + Number of B).

Mathematical representation of mutual interaction in sets A and B

In our methodology, we introduced a mathematical expression to quantify the mutual interaction between sets A and B. This expression captures the condition that an element in one set has at least one neighbor in the other set. We denoted this condition using the underscore symbol (_).

Let: N(A_B) be the number of elements in set A that have at least one neighbor in set B,
N(B_A) be the number of elements in set B that have at least one neighbor in set A,
N(A) be the total number of elements in set A,
N(B) be the total number of elements in set B.
The mutual interaction measure is expressed as:

$$M = \frac{N(A\_B)+N(B\_A)}{N(A)+N(B)}$$

Tissue partitioning for mutual interaction computation

In the context of tissue partitioning, the mutual interaction value is computed separately for cells in the tumour and stroma regions. This process involves considering points in the stroma (or tumour) from set "A" and computing the neighboring metric with all points in set "B" (not restricted to stroma only). Similarly, the measure is repeated for points in the stroma (or tumor) from set "B," computing the neighboring metric using all points in set "A." To ensure comparability, the computed values are normalized by the sum of points in sets "A" and "B" in stroma (or tumor). This normalization accounts for the varying cell densities in different tissue compartments, providing a more accurate assessment of mutual interactions. This approach allows for a nuanced understanding of cellular dynamics within specific tissue environments, considering the unique interactions occurring in both tumor and stroma regions.

Cellular triplets spatial interactions

Building upon the established function for pairwise interactions, our methodology extends seamlessly to analyze cellular triplets. Consider three sets of points: "A," "B," and "C," each representing distinct cell types.

For triplets, the mutual interaction is computed as follows:

$$M = \frac{N(A\_B\_C)+N(B\_A\_C)+N(C\_A\_B)}{N(A)+N(B)+N(C)}$$

Survival curves

Survival curves for overall survival (OS) in our clinical cohorts were constructed using the Kaplan–Meier estimator and statistical significance was determined using the log-rank test. For the NHS I/II study cohort a multivariate Cox proportional hazards regression model was used.

Targeted DNA analysis

UPENN and IMCOL primary-recurrent cohorts: DNA extraction and libraries preparation

Three sections of 8um-thick were freshly cut from each FFPE blocks. Tissues were deparaffinized with 500ul Deparaffinization solution (Qiagen) and total DNA was extracted with QiAmp DNA FFPE tissue kit (Qiagen). Final DNA was eluted in 25ul of ATE buffer. DNA concentration was measured with Qubit DNA fluorometer method (inVitrogen). A minimum of 80 ng of sample input (100ng preferred) was used to construct the targeted libraries with Archer VariantPlex somatic protocol for Illumina, following manufacturer's instructions. Reagents were supplied by ArcherDX, including our custom panel of 49 gene-specific primers that target regions of interest and Archer MBC adapters to tag each unique molecule with a barcode. Final libraries were quantified by Qubit DNA method and quality was checked on Fragment Analyzer (HS-NGS fragment kit, Agilent).

Sequencing and analysis

Libraries were pooled at equimolar concentrations and loaded into the Miseq or Novaseq Illumina system for sequencing, following ArcherDX recommendations. Fastq files generated were analyzed using Archer analysis software. The reads are aligned with BWA-MEM and PCR duplicates are removed. Single nucleotide variants and indels are identified using HaplotypeCaller for both tumor and three unmatched normal tissue samples. The mutations in tumor samples are cleaned by removing mutations that are also present in normal samples. Total read depth and variant allele frequency filters are applied to remove potential artifacts. Ambiguous mutations are cross checked using Archer mutation calling pipeline and only kept if they were reported in both pipelines. Mutations are

annotated with ClinVar to determine pathogenic variants. For identifying DSB repair pathway mutations only the truncating mutations, pathogenic mutations or damaging mutations according to both SIFT and PolyPhen are considered.

HiTide-UPENN primary cohort

Mutations in the TP53, BRCA1, BRCA2 and RAD51C genes and methylation of BRCA1 were identified as previously described[81–83] through BROCA targeted panel.

Bulk RNA sequencing library preparation and processing

Total RNA was extracted from snap frozen tissues. Tumor tissues were disrupted on ice in RLT buffer supplemented with ~40mM dithiothreitol (DTT, Sigma Aldrich), using a pestle (70 mm, 1.5/2.0 mL, Schuett-Biotec). Lysates were further homogenized using a syringe and needle. After centrifugation at full speed for 3 min in a benchtop centrifuge (Eppendorf) at 4°C, supernatant was used for RNA extraction according to manufacturer's protocol, including on column DNase digestion, using the RNeasy Mini Kit (Qiagen). RNA quality was assessed with a Fragment Analyzer (Agilent) and Nanodrop One spectrophotometer (Thermo Scientific). Quantification was performed with the Qubit RNA broad-range (BR) assay kit (Invitrogen). RNA sequencing libraries were prepared using the Illumina TruSeq Stranded RNA reagents according to the protocol supplied by the manufacturer and sequenced using HiSeq 4000/Novaseq. Illumina paired-end sequencing reads were aligned to the human reference GRCh37/hg19 genome using STAR aligner (version v2.7.3a; https://github.com/alexdobin/STAR) and the 2-pass method as briefly follows: the reads were aligned in a first round using the –runMode alignReads parameter, then a sample-specific splice-junction index was created using the –runMode genomeGenerate parameter. Finally, the reads were aligned using this newly created index as a reference. To transform raw counts into TPM values, raw counts were summarized at the gene level using htseq-count (version 0.9.1). Read counts where then normalized into reads per million (TPM). The comprehensive gene annotation version 32 was downloaded from the GENCODE website (https://www.gencodegenes.org/human/release_32lift37.html) and chromosome position, transcript structure and transcript and protein sequences were selected to annotate genes.

Gene expression analyses

Genes with zero expression and with low gene count variance were filtered out from the analysis and transcript per million, TPM, values were used for the downstream analysis. Additionally, genes sharing the same enzymatic function were collapsed using the geometric mean. Analysis was performed in R language for statistical computing. Gene set variation analysis enrichment scores were calculated using GSVA R package and subsequently clustered using Euclidean distance and ward.D2 method in with the pheatmap R package. The p-values in the boxplots were calculated using Wilcoxon test and were adjusted with the Bonferroni correction.

Gene signatures

The detailed description of the gene sets is provided in Table S2. More than half of the signatures were derived from the MSigDB database Hallmark collection (full) and C2 collection (selected signatures). About 10% of the signatures were compiled from the important signatures previously identified in our Lab (complete references are indicated in the table).

Mouse treatment

We injected 5 × 106 ID8 derivative ovarian cancer cells expressing luciferase (ID8Luc) i.p. in C57BL/6NHsd female mice. To mimic OC standard of care we treated mice with i.p. Carboplatin (20mg/kg) – Taxol (3mg/kg) once weekly for 6 weeks, reach tumor control (luciferase signal, +/-SEM) and then wait for tumor recurrence. Mouse health and welfare were monitored regularly. For both control groups and experiments evaluating survival post-therapy, we used body and health performance score sheets (taking into consideration ascites accumulation) and mice were sacrificed once reaching the equivalent of humane endpoints. Anti-CSF1R (400ug/mouse/injection bi-weekly), anti-IFNAR-1 (200ug/mouse/injection bi-weekly), anti-TREM2 (200ug/mouse/injection bi-weekly) and anti-PDL1 (200ug/mouse/injection bi-weekly) were all administered i.p. and detailed duration of the experiment treatment is reported in Figure 5 and respective figure legend. Celecoxib in granule (Sandoz, 200mg, from pharmacy) was weighed using a fine balance and made up in a 60:40 ratio of DMSO (1 part, Sigma)/PEG 300(5 parts, Sigma):dH_2O at a concentration of 3 mg/ml. 200 μl (30 mg/kg) was given by oral gavage every 2 days. Olaparib (40ug/g mouse) was given by oral gavage every day for the duration of the experiment.

Whole body Bioluminescence imaging

Tumor growth was monitored by Bioluminescent imaging (BLI). BLI was performed using the Xenogen IVIS® Lumina II imaging system and the photons emitted by the Luciferase-expressing cells within the animal body were quantified using Living Image software. Briefly, mice bearing ID8Luc cancer cells were injected i.p. with D-luciferin (150mg/kg stock, 100 μL of D-luciferin per 10 g of mouse body weight) resuspended in PBS and imaged under isoflurane anesthesia after 10 min. A 49 pseudocolor image representing light intensity (blue, least intense; red, most intense) was generated using Living Image. BLI findings were confirmed at necropsy.

Tumour processing and flow cytometry

At the time of sacrifice, i.p. tumors were dissected. Tumors were digested in 200 μg/ml Liberase TL and 5 units/ml DNase I in DMEM for 30min at 37°C, with rotation. For *ex vivo* staining, 1-2x10^6 cells were stained with Zombie UV Fixable Viability Kit (1:500, in PBS) for 15min on ice. Fc receptors were blocked for 10 min at 4°C with 5 μg/ml Mouse BD FC Block. Cells were fluorescently labeled with

antibodies, dilution 1:50, for 30 min at 4°C with PBS and 2% FBS, washed, fixed in fixation buffer (2% formaldehyde in PBS) and resuspended in PBS or intracellularly stained according to the manufacturer's protocol (eBiosciences). For intracellular staining, eBioscience Foxp3/Transcription Factor kit was used (Thermo Fisher Scientific). Cells were permeabilized and fixed 1 h in fix/perm buffer (Thermo Fisher) and intracellular staining was performed for 45 min at room temperature in perm buffer. After staining, cells were acquired on a five-laser Fortessa (BD Biosciences) with FACS DIVA software v.9.0 (BD Biosciences) and analyzed with FlowJo (TreeStar).

Single-cell RNA sequencing

Cells were counted on the ADAM automated cell counter and viability was estimated with the AccuStain solution kit (NanoEntek). Cells were surface-stained with CD45-BV785 + CD8-BU650 for 20min at 4°C and resuspend in 1ml of PBS+0.04% BSA (Sigma-Aldrich) after washing.

Cell multiplexing

After staining, samples were labeled and multiplexed by group, allowing to be pooled in a single GEM for encapsulation. Cell labeling was performed according to the Cell multiplexing oligo labeling protocol from 10x Genomics (CG00391). 500'000 cells per sample (if possible, otherwise minimum 200'000 cells) were labeled with a cell multiplexing oligo for 5min at room temperature. After two washes with PBS+ 1% BSA, cells were resuspended in PBS + 0.04% BSA + 0.1% RNasin and multiplexed by equimolar pools. Before sorting, 10min of viability staining with Reddot1 (Biotium) and 3min of DAPI staining were performed.

FACS sorting

50'000 total live cells were sorted for each pool on a MoFlo Astrios (Beckman Coulter) and collected in 0.2mL PCR tubes containing 10ul in PBS + 0.04% BSA + 0.1% RNasin. After sorting, cells were manually counted with hemacytometer, and viability was assessed using Trypan blue exclusion.

Encapsulation and library construction

Single-cell RNA libraries were generated using the Chromium Next GEM Single Cell 3' Library and Gel beads kit v3.1 according to the manufacturer's instructions. For each sample, 15'000 to 30'000 cells were loaded into the Chromium machine, encapsulated and barcoded following the manual (CG000388), aiming a recovery of 10'000 to 20'000 cells according to manufacturer conditions. After encapsulation and reverse transcription, 11 PCR cycles were used to amplify cDNA. All libraries construction steps were performed according to the manufacturer's protocol. For each sample, 3GEX library was generated. If sample was part of a pool, a Cell Multiplexing Library (CML) was also constructed. Complementary DNA and library quality were examined on a Fragment Analyzer (Agilent) and quantification was performed with the Qubit HS dsDNA assay kit (InVitrogen).

Sequencing

Barcoded 3'GEX libraries and CML were pooled and sequenced on an on Illumina HiSeq 4000 or NovaSeq6000 system, following 10X Genomics recommendations. GEX libraries were sequenced to a median depth of 20,000 unique reads per cell and Cell Multiplexing Oligos (CMO) libraries were sequenced to a median depth of 5'000 unique reads per cell.

Alignment, annotation and downstream analysis

Alignment, barcode and UMI counting were performed using mm10-2020-A reference genome and cellranger-6.1.1 multi from 10x Genomics. Multiple gene expression libraries were combined via *cellranger aggr* and filtered feature-barcode matrix containing gene expression data was further analyzed with the Seurat R package. The total number of cells detected was 50949, with number of cells successfully assigned to an individual mouse CMO library ranging between 15% and 85%. To rescue the cells that were not assigned to any CMO library (i.e. to any individual sample), the alignment procedure from above was repeated in *cellranger* without providing the CMO library information. Next, all the cells whose barcodes were not mapped to any of the CMO libraries, were pooled together for each corresponding mouse group as a pseudo-mouse and added to the resulting matrix for downstream analysis. For annotation purposes, several iterations were performed. In the first iteration, cells were clustered at a high resolution leading to a big number of cell clusters with shared properties. The clusters were obtained using the standardized Seurat procedure: data counts were log normalized using the *NormalizeData* function, then variable features were found using *vst* method and 600 fetures. Next, a linear transformation using the *ScaleData* function was applied, and linear dimensional reductions were calculated using *RunPCA* (for the principal component analysis) and *RunTSNE* (for the t-Distributed Stochastic Neighbor Embedding) functions with first ten principal components used as input features and perplexity of 30. Finally, shared nearest neighbors, SNN, was calculated using *FindNeighbors* (with 10 PCs and k=30) followed by *FindClusters* functions (with resolution = 20). Based on the known exclusive markers, the cells were automatically classified as immune (*Cd3g*, *Cd3d*, *Cd3e*, *Cd2*, *Cd8a*, *Cd8b1*, *Foxp3*, *Il2ra*, *Trbc1*, *Cd19*, *Ms4a1*, *Cd79a*, *Cd79b*, *Ncr1*, *Klrb1c*, *Klrd1*, *Klrk1*, *Aif1*, *Ms4a7*, *Cd14*, *Fcgr4*, *Itgam*, *Itgax*, *Mrc1*, *Cd163*, *Fcer1a*, *Clec10a*, *Mzb1*, *Derl3*), non-immune (*Epcam*, *Msln*, *Egfr*, *Fap*, *Pdpn*, *Dcn*, *Thy1*) or endothelial cells (*Pecam1*, *Fas*) if at least 80% of the cluster's cells expressed the markers. The cells within these 3 initial categories were further automatically classified as T cells (*Cd3g*, *Cd3d*, *Cd3e*, *Cd2*, *Cd8a*, *Cd8b1*, *Foxp3*, *Il2ra*, *Trbc1*), B cells (*Cd19*, *Ms4a1*, *Cd79a*, *Cd79b*), NK cells (*Ncr1*, *Klrb1c*, *Klrd1*, *Klrk1*), Myeloid cells (*Aif1*, *Ms4a7*, *Cd14*, *Fcgr4*, *Itgam*, *Itgax*, *Mrc1*, *Cd163*, *Fcer1a*, *Clec10a*, *Mzb1*, *Derl3*, *Cd48*), endothelial cells (*Pecam1*, *Fas*), malignant

(*Epcam*, *Msln*, *Egfr*, *Brca1*, *Brca2*, *Trp53*), fibroblasts (*Fap*, *Pdpn*, *Dcn*, *Thy1*, *Ankrd1*, *Mcam*, *Cd70*, *Pdgfra*, *Pdgfrb*, *Itga5*, *Mme*) if at least 50% of the cells expressed the markers. At the end of the initial classification, the expression of the above markers along with the additional list of markers was visualized using the *doHeatmap* function in each of the assigned classes to verify the validity of classifier. After the first iteration, a filtering step was applied individually on each of the identified lineage depending on the total distribution of that lineage population: number of genes from 250 to 3000-6000; number of reads 500 to 15000-40000; below 15% mitochondrial content and within 1-7.5 to 40% ribosomal content. This reduced the total number of cells by 15%. At the second iteration, for the filtered cells from each individual library, variable genes from the log-normalized counts were found using vst method and then the libraries were integrated using the anchoring technique described in "Stuart and Butler et al.".[84] As during the first iteration, integrated data was scaled and then passed to PCA, t-SNE, and SNN analyses for identifying clusters (with resolution = 0.3). Next, gene expression centroids (average gene expression profiles per cell type) method was applied using matrices from Zilionis et al.[38] for main and sub-populations to predict the cell type of each given cell. Following the centroids methods prediction, the cell annotation was refined per each individual cluster using its initial assignment, its predicted state, and expression of a particular known markers (like *Cd8* for $Cd8^+$ T cells and *Foxp3* for Tregs). This refinement completed the second iteration of the cell annotations. At the last iteration, based on the annotations obtained from second iteration, cells were divided and re-clustered in five main groups or lineages: T cells, B cells, Myeloid, Malignant and doublets. For each of the main lineages of cells, the CMO associated genes were filtered out from the analysis and the normalization to clustering (resolution = 0.3) steps were performed as described above. Then, differentially expressed genes (using the *FindAllMarkers* function) were identified for each cluster and signature scores were calculated for each cell using the *AUCell* R package and "in-house" signatures defined in Table S2, Additionally, centroids method was applied to predict the states from Barras et al.[3] for each cell. Once all the above metrics were calculated, the cells per each cluster were manually refined considering all the newly obtained metrics and the initial annotation. When necessary, clusters were re-assigned to the different main lineage to reflect the observed DE genes in these cluster and signatures expressed in corresponding cells. Also, due to the gene expression dropout issue, for the cells that clearly expressed T cell markers, but were double negative for *Cd8* and *Cd4* expression, the assignment to *Cd8* versus *Cd4* group was based on predicted value from the centroid algorithm and based on which group of cells they clustered with. In addition, when markers from multiple lineages were expressed on the same cells (e.g. $Cd8^+Cd79a^+$ cells), these cells were categorized as doublets and omitted from the downstream analysis. Finally, the copy number inference algorithm from *infercnv* R package was applied to all malignant cells to validate their malignant state. A total of 900 cells (300 cells each) randomly selected from T, B and myeloid compartments were used as a normal reference to infer the copy number changes of the tumor cells. The low number of the resulting inferred copy number variations in the normal cells and high number of those in tumor cells validated the correctness of malignant cell assignment. To visualize the inferred CNV in cells per chromosomal location, the Next-Generation Clustered Heat Map Viewer (NG-CHM, STAR Methods) was used. To assess the CNVs in the malignant cells quantitatively, the segmentation of the inferred data was applied and then the number of breakpoints per chromosome was calculated for each cell. To segment the data, the inferred values for genes in each chromosome were ordered based on their chromosomal location and were assigned to the same segment if the difference between the two values did not exceed 0.1%. The segmented representation of the CNVs was visualized using the Integrative Genomics Viewer (IGV, STAR Methods). The images for all other downstream analyses were produced either by the built-in functions from Seurat package or by ggplot2 package.

Gene metaprogram analysis of malignant cells

Mouse single-cell RNA sequencing data were used to identify gene metaprograms in malignant cells. The malignant cells were isolated and processed using the *geneNMF* R package (GeneNMF v0.6.0) on a Seurat object transformed with *SCTransform*. The non-negative matrix factorization (NMF) was performed with ndim=6 on the SCT assay, following the guidelines of a previously described approach (bioRxiv 2024, https://doi.org/10.1101/2024.05.31.596823). To identify optimal metaprograms, the *multiNMF* function was executed with a range of factors (k) from 4 to 10. Subsequently, the *getMetaPrograms* function was applied with nprograms=10 and min.confidence=0.3 which resulted in the identification of 9 robust metaprograms (MPs). These MPs were visualized using the *plotMetaPrograms* function. Gene set enrichment analysis (GSEA) was performed on the metaprograms using the *runGSEA* function, incorporating Reactome and Hallmark pathway collections. The five most significantly enriched pathways per metaprogram were selected and visualized using the *pheatmap* R package. Metaprogram scores were then calculated for individual cells using the *AddModuleScore_UCell* function from the *UCell* R package. To examine enrichment patterns, the average metaprogram scores were computed for each malignant cell subset and visualized using the *pheatmap* R package.

MultiNicheNet analysis

MultiNicheNet (MNN) (version 1.0.3) was utilized to explore the differences in ligand-receptor interactions. Throughout our analysis, we used the default parameters to look at the top 250 targets with minimum log-fold change of 0.5 and a fraction cut-off of 0.05. For the ligand-receptor analysis in the mouse dataset, we initially encompassed the major cell types involved (Table S4): B cells, CD8 and CD4 T cells, DC cells, macrophages, malignant cells and stromal cells from N=12 recurrent samples (6 $Brca1^{mut}$ and 6 $Brca1^{wt}$) for a total of 23'449 cells (12'595 in the $Brca1^{mut}$ and 10'854 in the $Brca1^{wt}$). Subsequently, we conducted a more focused investigation on the above samples targeting the most promising interactions from malignant cells, macrophages, and DCs cells, considering finer annotation (N=11'978 total cells, 5'379 in the $Brca1^{mut}$ and 6'599 in the $Brca1^{wt}$ respectively). Due to a higher abundance of samples per category, we maintained recommended parameters such as "adjusted p.value = TRUE" "empirical_pval = FALSE". We used the get_top_n_lr_pairs function to generate two key outputs: the top 50 scaled products of ligand and receptor expression within each

experimental group, enabling us to estimate their ligand activity and a regulatory network highlighting the top 150 ligand-target gene interactions. For visualization, we specifically selected the 50 best-predicted interactions (Figure 5H).

Multiplex chromogenic immunohistochemistry

The triple chromogenic immunohistochemistry assay was performed using the Ventana Discovery ULTRA automate (Roche Diagnostics, Rotkreuz, Switzerland). All steps were performed automatically with Ventana solutions except if specified otherwise. Dewaxed and rehydrated paraffin sections were pretreated with heat using the CC1 solution for 40 minutes at 95°C. Primary antibodies were applied and revealed sequentially either with a rat Immpress HRP (Ready to use, Vector laboratories Laboratories) or a rabbit UltraMap HRP followed by incubation with a chromogen (ChromoMap DAB, Discovery purple and Discovery Teal). A heat denaturation step was performed after every revelation. The primary antibodies sequence was: rat anti-CD11c, rat anti-CD8 and rabbit anti-PanCytokeratin. Sections were counterstained with Harris hematoxyline (J.T. Baker) and permanently mounted with Pertex (Sakura). For immunohistochemical quantification of $CD8^+$ cells and $CD11c^+$ cells, 10 × 10 tiled bright-field pictures of FFPE sections were taken at 100μm magnification to cover almost whole slide surface. Cell counts were obtained using ImageJ software.

ELISA

PGE2 level in supernatant from ID8 *Trp53*$^{-/-}$*Brca1*^{wt} and *Trp53*$^{-/-}$*Brca1*^{mut} mouse OC cell lines was determined using PGE2 ELISA Kit (Cayman chemical, 514010) according to the manufacturer's instructions. PGE2 levels were measured by ELISA at 24, 48 and 72 hours. PGE2 concentrations were normalized to total number of live cells at each time point.

QUANTIFICATION AND STATISTICAL ANALYSIS

All statistical tests were performed using R (version 3.3.0) and GraphPad Prism softwares. All statistical details of experiments can be found in the figure legends, figures and results, including the statistical tests used, exact value of n, what n represents (e.g., number of technical and biological replicates, number of animals, etc.), definition of mean or median, and dispersion and precision measures (SD, SEM, confidence intervals).